

1 Global runoff partitioning based on Budyko- 2 constrained machine learning

3 Shujie Cheng^{1,2}, Petra Hulsman², Akash Koppa², Hylke E. Beck³, Lei Cheng¹, and
4 Diego G. Miralles²

5 ¹State Key Laboratory of Water Resources and Hydropower Engineering Science, Wuhan
6 University, Wuhan 430072, China

7 ²Hydro-Climate Extremes Lab (H-CEL), Ghent University, Ghent, Belgium

8 ³King Abdullah University of Science and Technology, Thuwal, Saudi Arabia

9

10 Correspondence to: Lei Cheng, lei.cheng@whu.edu.cn

11 Diego Miralles, Diego.Miralles@UGent.be

12

13

14 Highlights:

15 1. A Budyko-constrained machine learning approach is developed for
16 estimating long-term mean runoff and baseflow.

17 2. The hybrid approach performs well in terms of both the runoff coefficient
18 ($R^2=0.93$) and the baseflow coefficient ($R^2=0.84$).

19 3. Globally, 30% of the precipitation is partitioned into runoff, with baseflow
20 contribution estimated to be twice the quickflow (20.6% vs. 9.7%).

21 4. Primary drivers of runoff partitioning vary in space with topography and soil
22 properties as dominant factors.

23

24 **Abstract:** Understanding the partitioning of runoff into baseflow and quickflow
25 is crucial for informed decision-making in water resources management, guiding the
26 implementation of flood mitigation strategies, and supporting the development of
27 drought resilience measures. Methods that combine the physically-based Budyko
28 framework with machine learning (ML) have shown promise in estimating global
29 runoff. However, such 'hybrid' approaches have not been used for baseflow estimation.
30 Here, we develop a Budyko-constrained ML approach for baseflow estimation by
31 incorporating the Budyko-based baseflow coefficient (BFC) curve as a physical
32 constraint. We estimate the parameters of the original Budyko curve and the newly
33 developed BFC curve based on 13 climatic and physiographic characteristics using
34 boosted regression trees (BRT). BRT models are trained and tested in 1226
35 catchments worldwide and subsequently applied to the entire global land surface at a
36 0.25° grid scale. The catchment-trained models exhibit strong performance during the
37 testing phase, with R^2 values of 0.96 and 0.88 for runoff and baseflow, respectively.
38 Results reveal that, on average, 30.3% (spatial standard deviation std=26.5%) of the
39 continental precipitation is partitioned into runoff, of which 20.6% (std=22.1%) is
40 baseflow and 9.7% (std=10.3%) is quickflow. Among the 13 climatic and
41 physiographic characteristics, topography and soil-related characteristics generally
42 emerge as the most important drivers, although significant regional variability is
43 observed. Comparisons with previous datasets suggest that global runoff partitioning
44 is still highly uncertain and warrants further research.

45

46 Keywords: runoff partitioning, baseflow, quickflow, Budyko, machine learning

47

48 1 Introduction

49 Accurate partitioning of runoff (Q) into its main components – baseflow (Q_b) and
50 quickflow (Q_q) – is crucial for water management and emergency planning during
51 droughts (Apuv & Cai, 2020) and floods (Roxy et al., 2017). Baseflow, sometimes
52 referred to as 'slow flow', provides most of the water for sustaining river flows during
53 dry periods (Miller et al., 2016). It originates from groundwater and other delayed
54 sources, such as wetlands, lakes, melting of snow and ice (Hall, 1968). Quickflow is
55 directly responsible for flood generation (Yin et al., 2018), and is a result of fast
56 processes such as saturation or infiltration of excess overland flow and fast subsurface
57 flow, i.e., processes where precipitation is not retained in the soil (Beven & Kirkby,
58 1979). Process-based models play an important role in accurately estimating global
59 runoff, quickflow and baseflow; this includes among others land surface models
60 (LSMs) and global hydrological models (GHMs). Nonetheless, LSMs and GHMs
61 struggle with runoff partitioning resulting in poor performances in terms of baseflow
62 index ($BFI = Q_b/Q$) – see e.g. Beck et al. (2017).

63 To complement process-oriented models, data-driven machine learning (ML)
64 techniques have been developed to assess runoff partitioning regionally and globally
65 without the biases induced by process-based models. For instance, Huang et al. (2021)
66 adopted a random forest model (RF) and multiple linear regression approach to
67 estimate the baseflow index ($BFI = Q_b/Q$) in the United States. Beck et al. (2013,
68 2015) achieved satisfactory performance for BFI estimation globally ($R^2=0.65$) and
69 provided global BFI datasets by using neural networks to relate BFI to
70 climatic/physiographic characteristics. ML has the potential to build effective
71 relationships between inputs and outputs, even if underlying physical processes are
72 unknown. That is why ML has been growing in popularity in hydrological sciences
73 beyond runoff (Xie et al., 2021), being used to predict evaporation (Jung et al., 2010)
74 and precipitation (Sadeghi et al., 2019; Beck et al., 2010) as well. Despite the strength
75 of pure ML models, the major limitation is their “black box” nature, and hence their
76 lack of physical constraints and limited interpretability. The combination of
77 physically-based models and ML methods, i.e., 'hybrid' approaches, can retain both of
78 their individual strengths (de Bézenac et al., 2019; Koppa et al., 2022; Kraft et al.,
79 2022; Zhao et al., 2019). Hence, these physically-constrained ML methods can
80 potentially improve the realism of the runoff partitioning estimates globally.

81 Previous studies have illustrated the advantage of the Budyko (1961) framework
82 as a physical constraint for pure ML to estimate runoff (Bai et al., 2020; Liu & You,
83 2021), while no such attempt has been made for baseflow estimation yet. Recently,
84 the Budyko framework was expanded by Cheng et al. (2021) to partition baseflow
85 from precipitation with the Budyko-based baseflow coefficient (BFC) curve. This
86 enables the Budyko framework to provide consistent physical constraints for both
87 runoff and baseflow estimation. Both the Budyko and BFC curves depend on the
88 aridity index and use lumped parameters (parameter α in Fu's equation and $Q_{b,p}$ in the
89 BFC curve, see Section 2.1) to incorporate climatic and physiographic properties such
90 as vegetation, soil, topography, and human activities (Mianabadi et al., 2020; Potter et
91 al., 2005; Tang & Wang, 2017; Zhang et al., 2001). Zhang et al. (2001) revealed the
92 impact of vegetation change on long-term evaporation and suggested α equal to 0.5
93 and 2.0 for herbaceous plants and trees, respectively. Besides vegetation, Liu et al.
94 (2018) indicated that climate seasonality also plays an important role on the Budyko
95 parameter α . More complex relationships have also been proposed for small
96 catchments (Bai et al., 2020). These different relationships between α and catchment
97 properties indicate that a detailed understanding of the Budyko parameter is yet to be
98 achieved (Padrón et al., 2017). ML models have the strength to achieve better
99 regionalization of the parameters within the Budyko and BFC curves.

100 In this study, we design a framework for the long-term partitioning of global
101 runoff by adopting the Budyko and Budyko-based BFC curves as physical constraints
102 for ML models. The hybrid Budyko–ML approach makes full use of the available
103 data, and enables physical consistency by obeying the Budyko limits of water and
104 energy conservation. The primary objectives are to (1) develop Budyko constrained
105 ML models to estimate individual runoff components globally, (2) assess the accuracy
106 of the different estimated components, (3) analyse their spatial patterns, and (4)
107 identify and quantify the primary drivers of runoff partitioning. The derived dataset
108 includes gridded total runoff (Q), baseflow (Q_b), quickflow (Q_q), runoff coefficient
109 ($\text{RFC}=Q/P$), baseflow coefficient ($\text{BFC}=Q_b/P$), and quickflow coefficient
110 ($\text{QFC}=\text{RFC}-\text{BFC}$) at 0.25° resolution. The structure of the paper is as follows:
111 Section 2 describes the data development process, Section 3 describes the input
112 datasets, and Sections 4 and 5 present the results and discussions, respectively.

113 2 Methods

114 2.1 Budyko curve for runoff estimation

115 The Budyko framework is a first order approach that partitions long-term mean
116 precipitation into runoff and actual evaporation (Budyko, 1961). According to this
117 framework, both fluxes are limited by the water supply (typically precipitation, P) and
118 the energy demand on evaporation (typically potential evaporation, E_p). This
119 framework assumes that long-term soil water storage changes are negligible. Hence,
120 the water balance can be written as:

$$121 \quad P = E_a + Q \quad (1)$$

122 where P is precipitation, Q is runoff and E_a is actual evaporation.

123 As the original Budyko (1961) equation does not consider climatic and
124 physiographic properties, several studies proposed alternative equations that introduce
125 a single parameter to incorporate these properties (Choudhury, 1999; Yang et al.,
126 2007; Zhang et al., 2001). The formulation proposed by Fu (1981) and Zhang et al.
127 (2004) is adopted in this study:

$$128 \quad \frac{E_a}{P} = 1 + \frac{E_p}{P} - \left[1 + \left(\frac{E_p}{P} \right)^\alpha \right]^{\frac{1}{\alpha}} \quad (2)$$

129 By combining Eq.1 and Eq.2, the equation for Q estimation can be written as:

$$130 \quad \frac{Q}{P} = 1 - \frac{E_a}{P} = -\frac{E_p}{P} + \left[1 + \left(\frac{E_p}{P} \right)^\alpha \right]^{\frac{1}{\alpha}} \quad (3)$$

131 where α is a parameter reflecting the secondary controls such as climate variability,
132 vegetation, soil and topography, and can range from 1 to ∞ (Zhang et al., 2004). High
133 α values result in low runoff and high actual evaporation for specific precipitation and
134 potential evaporation values (Figure 1a). Figures in this study visualise P/E_p instead
135 of E_p/P to put more focus on humid regions with larger variability of Q/P .

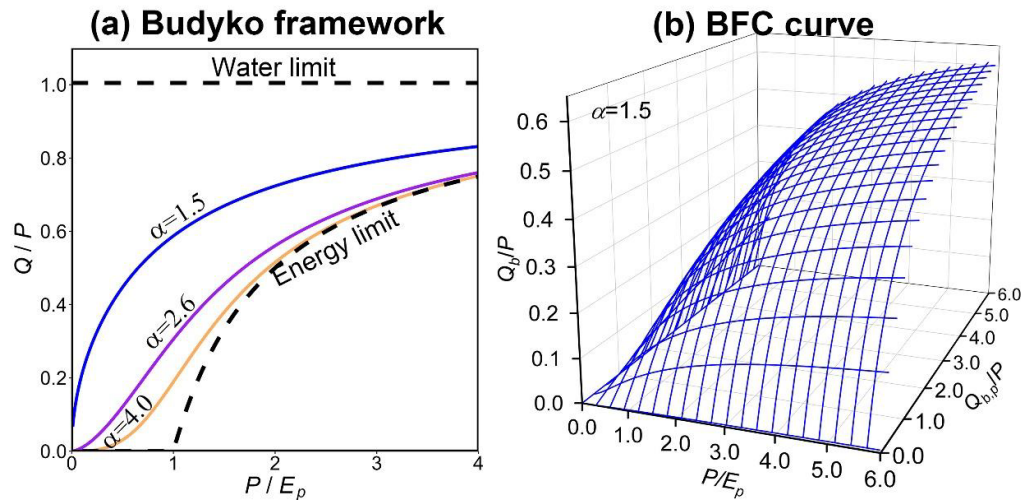
136 2.2 BFC curve for baseflow estimation

137 The BFC curve was developed by Cheng et al. (2021) to estimate long-term
138 mean baseflow (Q_b) based on the Budyko framework with suitable modifications (see
139 supplementary material). The BFC equation (Eq. 4) indicates that the baseflow not
140 only depends on P and potential evaporation E_p , but also on the potential baseflow

141 ($Q_{b,p}$). This latter parameter is newly introduced in this study and indicates the
 142 amount of baseflow that would occur if sufficient water were available. Hence, it is an
 143 upper limit for the baseflow, analogous to the concept of E_p for the case of
 144 evaporation. See the supplementary material for the derivation of the equation, which
 145 is slightly modified compared to Cheng et al. (2021). The final equation of the BFC
 146 curve is as follows:

$$147 \quad \frac{Q_b}{P} = \frac{Q_{b,p}}{P} + \left[1 + \left(\frac{E_p}{P}\right)^\alpha\right]^{\frac{1}{\alpha}} - \left[1 + \left(\frac{E_p}{P} + \frac{Q_{b,p}}{P}\right)^\alpha\right]^{\frac{1}{\alpha}} \quad (4)$$

148 where α is a parameter (identical to the one in Eq. 3). Q_b/P increases with increasing
 149 P/E_p and $Q_{b,p}/P$. High $Q_{b,p}$ values result in high baseflow and low quickflow for
 150 specific precipitation and potential evaporation values (Figure 1b).



151

152 Figure 1. Visualization of the physical constraints for (a) runoff, Budyko curve (Eq. 3), and
 153 (b) baseflow, BFC curve (Eq. 4).

154 2.3 Calibration of parameters

155 The Budyko and BFC curves include the following two parameters: α and $Q_{b,p}$.
 156 The latter is also parameterized, since its value cannot be determined with any
 157 available dataset. For individual catchments, the parameter α is calibrated first by
 158 using the Budyko curve (Eq. 3) and observed long-term mean Q , P , and E_p . Then,
 159 $Q_{b,p}$ is calibrated using the BFC curve (Eq. 4) and observed long-term mean Q_b , P , E_p ,
 160 and α (as calibrated in the previous step).

161 **2.4 Machine learning to relate parameters to climatic and**
162 **physiographic properties**

163 The parameters (α and $Q_{b,p}$) are regionalized as functions of climatic and
164 physiographic properties using ML. The calibrated α and $Q_{b,p}$ in each catchment (see
165 Section 2.3) serve as a benchmark for training ML models. The catchment-trained ML
166 models are then used to regionalize α and $Q_{b,p}$ globally at grid scale.

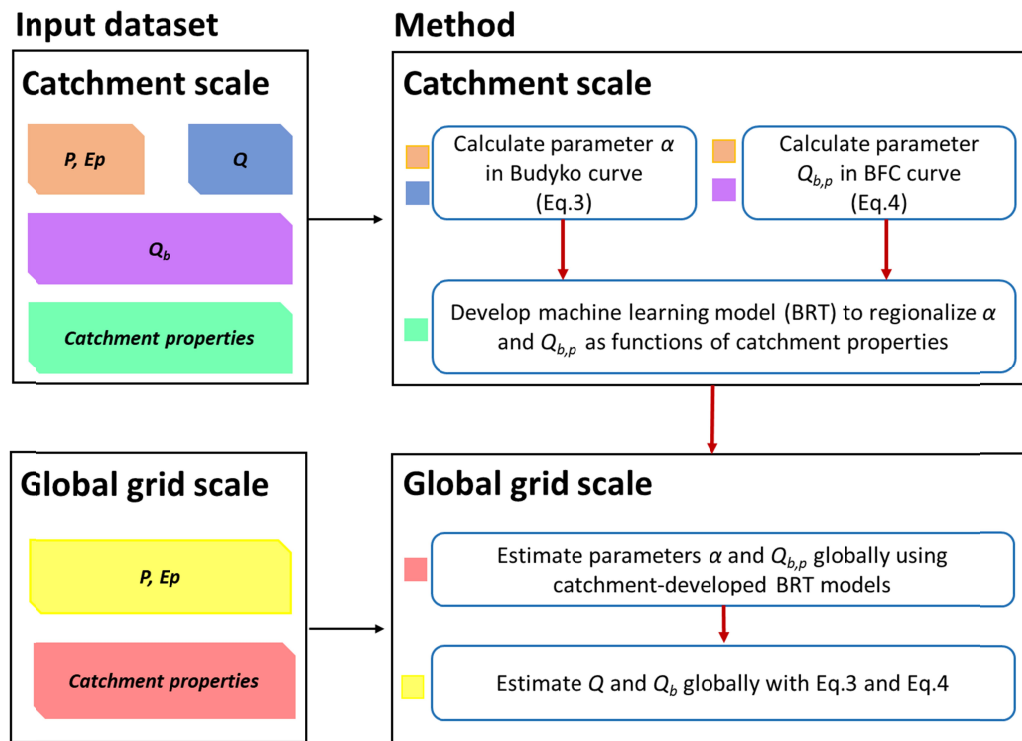
167 This study uses Boosted Regression Trees (BRT), which combines the strengths
168 of a regression tree algorithm and a boosting algorithm (Elith et al., 2008). BRT
169 differs fundamentally from conventional techniques that aim to produce a single “best”
170 parsimonious model, as it constructs multiple regression models in the algorithm
171 (Elith et al., 2008). The process of training a BRT model includes two parts:
172 regression trees and a boosting algorithm. First, multiple regression trees are built by
173 minimizing the prediction errors. Second, the boosting algorithm combines the
174 regression trees to give improved predictive performance. An effective strategy for
175 fitting a single decision tree is to grow a large tree, and then to prune it by collapsing
176 the weakest links as identified through cross-validation (Franklin, 2008). The first
177 regression tree is grown using recursive binary splits, that is, a binary split is
178 repeatedly applied to its own output until the loss function is maximally reduced. The
179 second tree is fitted to the residuals of the first tree, and the second tree can contain
180 quite different variables and split points. Consequently, multiple trees are fitted
181 additively based on the residuals of the previous tree. For multiple fitted trees, the
182 boosting algorithm averages trees to increase model performance. The dominant
183 drivers for the parameters α and $Q_{b,p}$ are estimated through method local interpretable
184 model-agnostic explanations (LIME) (Ribeiro et al., 2016).

185 Several hyper-parameters in BRT can be adjusted, including tree complexity (tc),
186 learning rate (lr) and bag fraction (bf). To find the most robust model for our analysis,
187 combinations of the following parameter values are tested using a 10-fold cross-
188 validation strategy: $tc \in \{4, 7, 10, 12\}$, $lr \in \{0.0005, 0.005, 0.01\}$ and $bf \in \{0.4, 0.5, 0.6,$
189 $0.8\}$ (Elith et al., 2008). The combination of hyper-parameter values with the highest
190 test performance is $tc=12$, $lr=0.01$, and $bf=0.50$. 10-fold cross-validation strategy is
191 also used for training models. The training is conducted ten times. Each time, 10
192 groups of catchments are randomly formed, of which nine groups are used for training
193 and one for testing. Ten BRT models are finally constructed at catchment scale and

198 then applied at grid scale globally. 10 maps of α and $Q_{b,p}$ are produced, and hence 10
 199 maps of Q and Q_b . The mean values of the 10 maps are computed as a final result,
 200 with the uncertainty calculated as the standard deviation of the 10 BRT models shown
 201 in supplementary Figure S3.

199 2.5 Overview of the modelling process

209 The methods and input datasets used in this study are summarized in Figure 2.
 210 Global runoff partitioning maps are developed with the following steps: First,
 211 parameters α and $Q_{b,p}$ in Eq.3 and Eq.4 are calibrated at catchment level (see Section
 212 2.3). This step uses Q , Q_b , P and E_p data at the catchment level. Q_b is extracted from
 213 Q using the digital filter method (see Section 3.1). Next, BRT models are developed
 214 at the catchment level to relate α and $Q_{b,p}$ to various climatic and physiographic
 215 properties. This step applies a 10-fold cross-validation strategy, resulting in 10 BRT
 216 models. The BRT models are then used to estimate α and $Q_{b,p}$ globally at grid scale.
 217 Finally, Q and Q_b are estimated globally using Eq. 3–4, P and E_p data, and the BRT-
 218 derived parameters α and $Q_{b,p}$ as inputs.



210

210 Figure 2. Overview of the modelling process and input datasets. The input datasets required in
211 each step are indicated by the colored squares; they correspond to the input datasets listed on
212 the left.

213 3 Data

214 3.1 Observed runoff, baseflow and quickflow

215 Observed daily discharge data from 3274 gauge-stations are obtained from the
216 Global Runoff Data Centre (GRDC) dataset together with the corresponding
217 catchment boundaries (<https://www.bafg.de/GRDC/>). A set of 1314 gauge-stations
218 and their corresponding catchments are selected from the initial dataset based on the
219 following requirements. First, the record length needed to be at least 10 years to allow
220 analyses on long-term mean values. Second, the missing data rate should be smaller
221 than 20% to warrant the representativeness of the mean values. Third, the water
222 balance should close, i.e., $|\frac{P - E_a - Q}{P}| < 0.1$, to exclude stations with too large data
223 uncertainties, or regional groundwater export/import as this is not included in the
224 Budyko framework. The spatial distribution of the selected 1314 catchments is shown
225 in Figure 3c.

226 Daily Q_b and quickflow ($Q_q = Q - Q_b$) are separated from daily Q using a digital
227 filter technique, more specifically the Lyne–Hollick (LH) method (Lyne & Hollick,
228 1979). Different digital filter methods have no significant influence on the long-term
229 estimation of Q_b and Q_s (Chen et al., 2023). The LH method has the advantage of
230 being minimally parameterized, and thus is easily applicable to a large sample of
231 catchments. The filter parameter f_i , also called recession constant, affects the degree
232 of attenuation. The number of passes determines the degree of smoothing, with the
233 backward pass nullifying the phase distortion from the forward pass. Here, the LH
234 method is applied in a conventional way with three passes (forward, backward, and
235 forward again) and the filter parameter f_i is set to 0.925 (Nathan & McMahon, 1990).

236 Long-term mean Q , Q_b and Q_q are estimated from their daily values and used to
237 estimate the catchment runoff coefficient ($\text{RFC} = Q/P$), baseflow coefficient
238 ($\text{BFC} = Q_b/P$), and quickflow coefficient ($\text{QFC} = \text{RFC} - \text{BFC}$). Note that the time period
239 for P , E_p , Q , Q_b and Q_q are consistent within each catchment by selecting their
240 crossing period. The available data lengths of the 1314 catchments vary from 10 to 41
241 years.

242 3.2 Climatic and Physiographic Characteristics

243 **Table 1** lists 16 climatic and physiographic variables that are used in this study,
 244 including the respective references, original spatial resolution and temporal coverage.
 245 In this study, analysis is done at 0.25° resolution; hence, observations are resampled
 246 to 0.25° using bilinear interpolation method when needed. Among the 16 variables,
 247 precipitation (P), potential evaporation (E_p) and evaporation (E_a) are direct inputs in
 248 the Budyko and BFC curves (Eq. 3 and 4). The remaining 13 variables are predictors
 249 for parameters α and $Q_{b,p}$ during the ML step (see Section 2.4). Three of these
 250 characteristics are related to climate, four to vegetation, three to topography, two to
 251 soil and one is related to human activities.

252 **Table 1.** Gridded climatic and physiographic characteristics used directly in the Budyko and
 253 BFC curve (P , E_a and E_p), or to predict runoff and baseflow with ML (remaining variables).

| Subcategory | Data | Description | Data Sources | Original Resolution | Temporal coverage |
|-------------|-------|--|---|---------------------|-------------------|
| Climate | P | Precipitation | MSWEP v1.1 (Beck et al., 2017) | 0.25° | 1980–2020 |
| | E_p | Potential Evaporation | TerraClimate (Abatzoglou et al., 2018) | 1/24° | |
| | E_a | Actual evaporation | GLEAM v3.6 (Martens et al., 2017) | 0.25° | |
| | TC | Air temperature | ERA5 (Hersbach et al., 2020) | 0.25° | |
| | SAI | Seasonality and asynchrony index | Calculated from daily P and E_p (Liu et al., 2018) | 0.25° | |
| | SWE | Snow water equivalent | GLOBSNOW L3av2 and NSIDC v0.1 (Armstrong, 2005; Luoju et al., 2013) | 0.25° | |
| Vegetation | NDVI | Normalized difference vegetation index | MODIS (https://modis.gsfc.nasa.gov/) | 0.05° | 2000–2014 |
| | WUE | Water use efficiency | | | |
| | LAI | Leaf area index | | | |
| | RD | Maximum rooting depth | Fan et al. (2017) | ~1km | Static |
| Topography | CTI | Topographic index | Marthews et al. (2015) | 500m | Static |
| | ELEV | Mean | Yamazaki et al. (2019) | 90m | |

| | | | | | |
|------------------|------|--|-------------------------------------|-------|-----------|
| | | elevation | | | |
| | SLO | Slope | Amatulli et al. (2018) | 1km | |
| Soil | STHI | Average soil and sedimentary deposit thickness | Pelletier, J.D, et.al, (2016) | 1km | Static |
| | SPO | Soil porosity | SoilGrids 2.0 (Poggio et al., 2021) | 250 m | |
| Human activities | HFP | Human influence index | Eric W. Sanderson et al. (2002) | 1km | 1995–2004 |

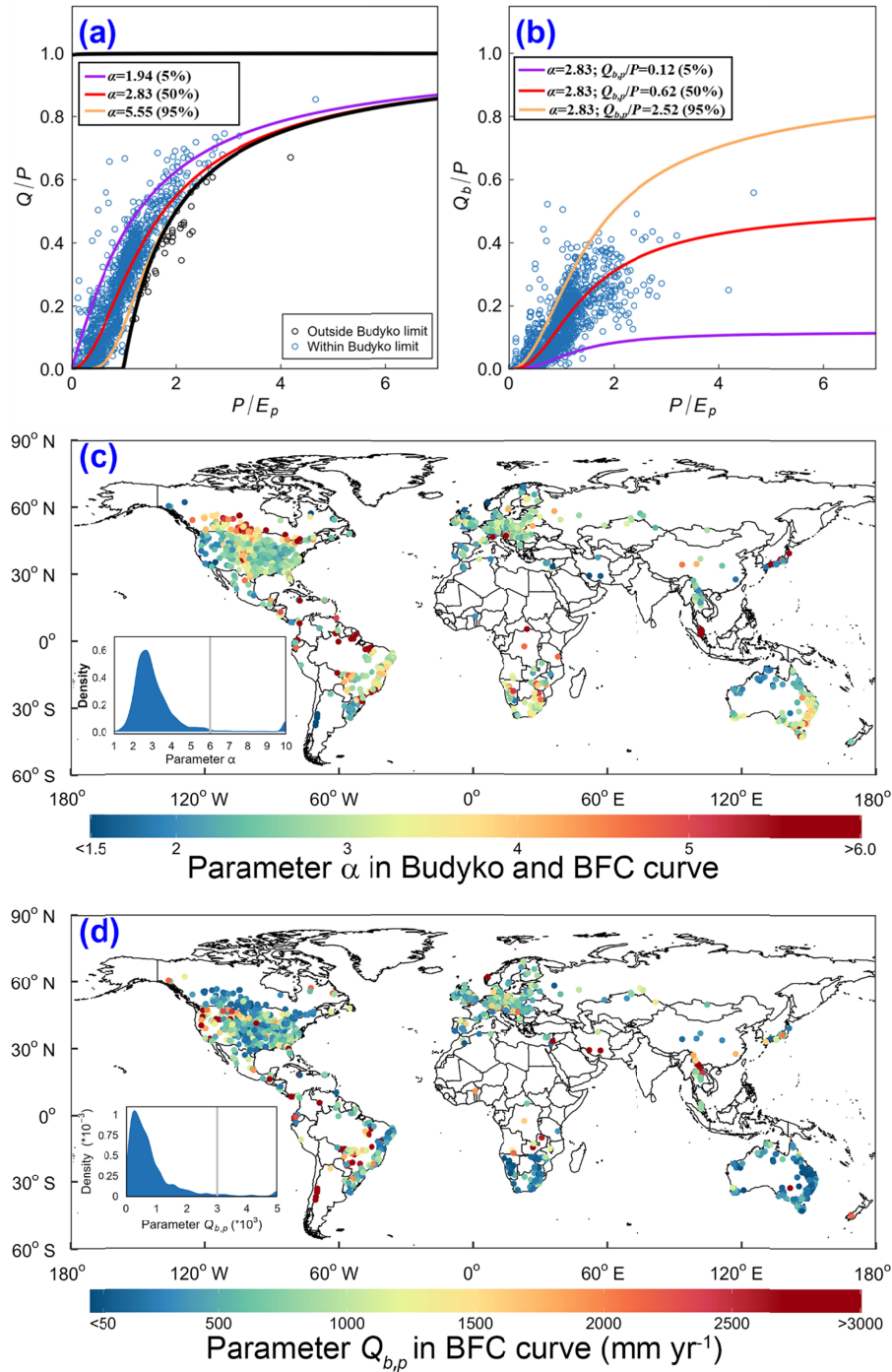
254

255 4 Results

256 4.1 Calibrated parameters at catchment scale

257 Figure 3 visualises the values of the parameters α and $Q_{b,p}$ for all 1314
258 catchments as calibrated with Eq. 3 and 4. Due to the large variability of catchment
259 conditions, the parameter values vary such that their 5% and 95% quantiles range
260 between $\alpha = 1.94\text{--}5.55$ and $Q_{b,p} = 104\text{--}2242 \text{ mm yr}^{-1}$, resulting in different Budyko
261 and BFC curves as shown in Figure 3a and b with the purple and orange lines. The
262 median values of the catchment-specific α and $Q_{b,p}$ are 2.83 and 547 mm yr^{-1} ,
263 respectively. The large variability of α and $Q_{b,p}$ is spatially shown in Figure 3c and d,
264 respectively. Large α values (i.e., $\alpha > 4$) mainly appear in the Great Plains in North
265 America, the east coast of Australia and South America. A mix of low and median α
266 values (i.e., $\alpha < 3$) appear in Europe and in the east of the United States. For the
267 spatial distribution of $Q_{b,p}$, Australia, southern Africa and the middle of the United
268 States show low $Q_{b,p}$ values. There are no obvious spatial patterns elsewhere. Of the
269 1314 catchments, 88 stations show extreme parameter values (i.e., $\alpha > 6.0$ and
270 $Q_{b,p} > 3000$; see the tails in the density plots in Figure 3c and d). In addition, 38
271 stations of these 88 stations fall outside the Budyko limits (i.e., $\alpha \rightarrow \infty$) as shown in
272 Figure 3a. These 88 stations with extreme parameter values are considered as outliers
273 and are therefore excluded, such that 1226 stations are left for the remainder of the
274 analysis. These remaining stations are further tested by analysing results during
275 calibration and validation periods (see Figure S1). For each catchment, the first 20
276 years are used to calibrate the parameters α and $Q_{b,p}$, and the remaining years are used

282 for validation. Catchments with less than 30 years of data are not validated. The
 283 validated runoff and baseflow show a correlation (R^2) of 0.95 and 0.94, respectively.
 284 The high validation performance illustrates that the Budyko and BFC curve with the
 285 calibrated α and $Q_{b,p}$ can reproduce the spatial variability of Q and Q_b well at the
 286 selected catchments.

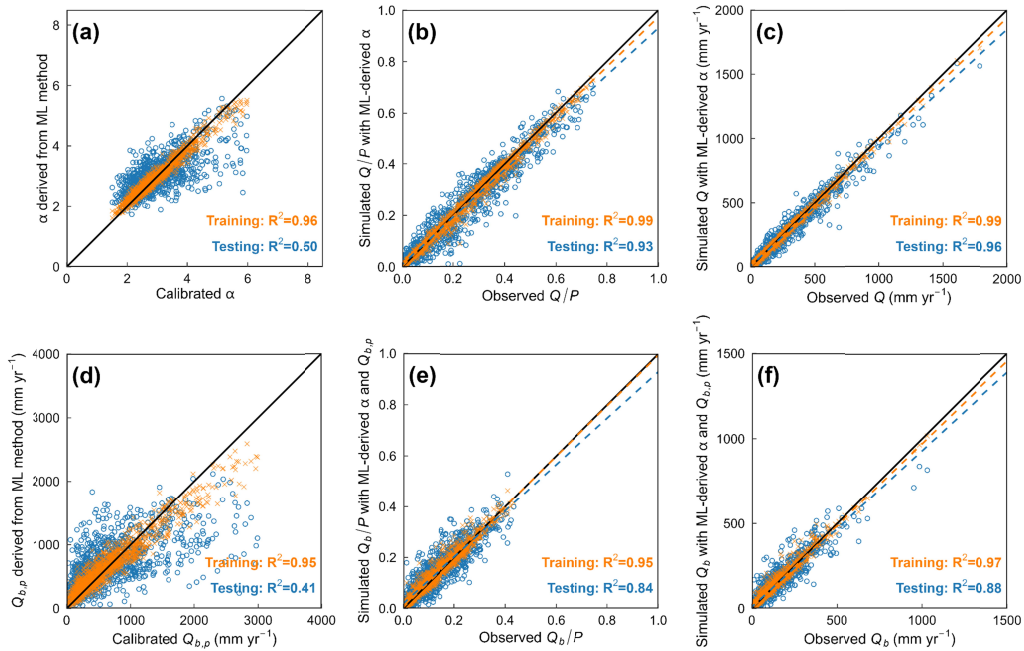


283 Figure 3. Scatterplots of (a) Q/P and (b) Q_b/P versus P/E_p . The lines in panel (a) and (b) are
284 the Budyko and BFC curves, respectively, using the following quantile values for the
285 parameters α and $Q_{b,p}$: 5% (purple), 50% (red), and 95% (orange). Note, that in (b) α is fixed
286 to its median value of 2.83 to focus on $Q_{b,p}$ changes. Spatial distribution and density plots of
287 (c) α and (d) $Q_{b,p}$. Extreme values beyond the grey lines in the density plots are considered as
288 outliers and are removed.

289 4.2 Catchment-scale performance of trained models

290 The first row in Figure 4 shows the performances of BRT-derived α , Q/P and Q
291 using Eq.3 and BRT-derived α (Budyko–ML). During training, all three variables
292 agree well with observations with RMSE for Q/P and Q equal to 0.02 and 17 mm yr⁻¹,
293 respectively (Figure 4b and c). During testing, the performances decrease as expected,
294 especially for α , with $R^2 = 0.50$. The performances of Q/P and Q remain high though,
295 with $R^2 = 0.93$ and 0.96 and RMSE = 0.04 and 46 mm yr⁻¹, respectively.

296 Similar to runoff, the second row in Figure 4 shows the performances of BRT-
297 derived $Q_{b,p}$, Q_b/P and Q_b estimated with Eq. 4 and BRT-derived α and $Q_{b,p}$. The
298 performance for these three variables is high during training, with $R^2 = 0.92$, 0.96 and
299 0.97, respectively (Figure 4d, e and f). The performance of $Q_{b,p}$ decreases during the
300 testing phase ($R^2=0.41$). As a result, also Q_b/P and Q_b perform slightly worse during
301 testing, but their performances are still acceptable, with R^2 for Q_b/P and Q_b equal to
302 0.84 and 0.88, respectively. The good performances of runoff and baseflow during the
303 testing phase indicates that the trained ML models for α and $Q_{b,p}$ at catchment scale
304 are reliable for estimating runoff and baseflow globally.



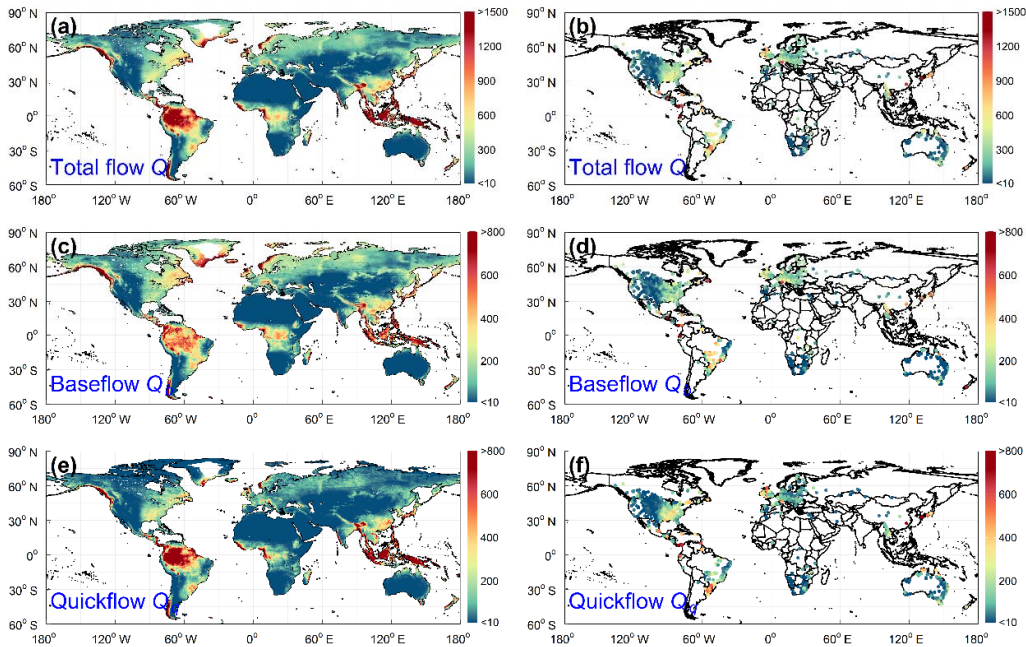
306

310 Figure 4. Performance of parameters α and $Q_{b,p}$ (a and d) from BRT models, Q/P (b), Q_b/P
 311 (e), Q (c) and Q_b (f) using the Budyko framework and BFC curve at catchment scale. Each
 312 point represents a catchment ($n=1226$ in each panel). The orange and blue lines are linear
 313 regression lines and the black lines mark the 1:1 relation.

311 4.3 Global map of runoff partitioning

325 The catchment-trained BRT models are applied globally to estimate parameters α
 326 and $Q_{b,p}$ on grid-scale. The spatial distribution of α and $Q_{b,p}$ is shown in Figure S2.
 327 Figure 5a, c and e illustrate the global, Budyko-based Q , Q_b and Q_q . This is compared
 328 to observations in Figure 5b, d, and f, respectively. The estimated global values show
 329 very similar spatial patterns to the observations. High flows appear at medium
 330 latitudes near the equator (30°N–30°S), while low flows are located at high latitudes
 331 (30°N–90°N and 30°S–60°S). Northern Africa and western Asia are exceptions, as
 332 they show low values at medium latitudes. Similarly, exceptions at high latitudes
 333 appear in regions near the coast of Chile, Europe and Canada where high runoff is
 334 found in the estimated maps (Figure 5a, c and e). The uncertainty for each variable (α ,
 335 $Q_{b,p}$, Q/P , Q_b/P , Q , and Q_b), which is considered equal to the standard deviation in the
 336 10 BRT models, is shown in Figure S3. The spatial uncertainty is equal to 0.13 for α ,
 337 114 mm yr $^{-1}$ for $Q_{b,p}$, 0.009 for Q/P , 0.01 for Q_b/P , 5.78 mm yr $^{-1}$ for Q , and 10.9 mm
 338 yr $^{-1}$ for Q_b . The uncertainty is larger for Q_b than Q since Q only relies on one

325 parameter (α), while Q_b relies on two parameters (α and $Q_{b,p}$). Overall, the global,
 326 long-term mean annual Q is on average 274 (std=418) mm yr⁻¹, Q_b 151 (std=181)
 327 mm yr⁻¹ and Q_q 123 (std=270) mm yr⁻¹. The results illustrate that the global river
 328 supply relies more on baseflow than quickflow.



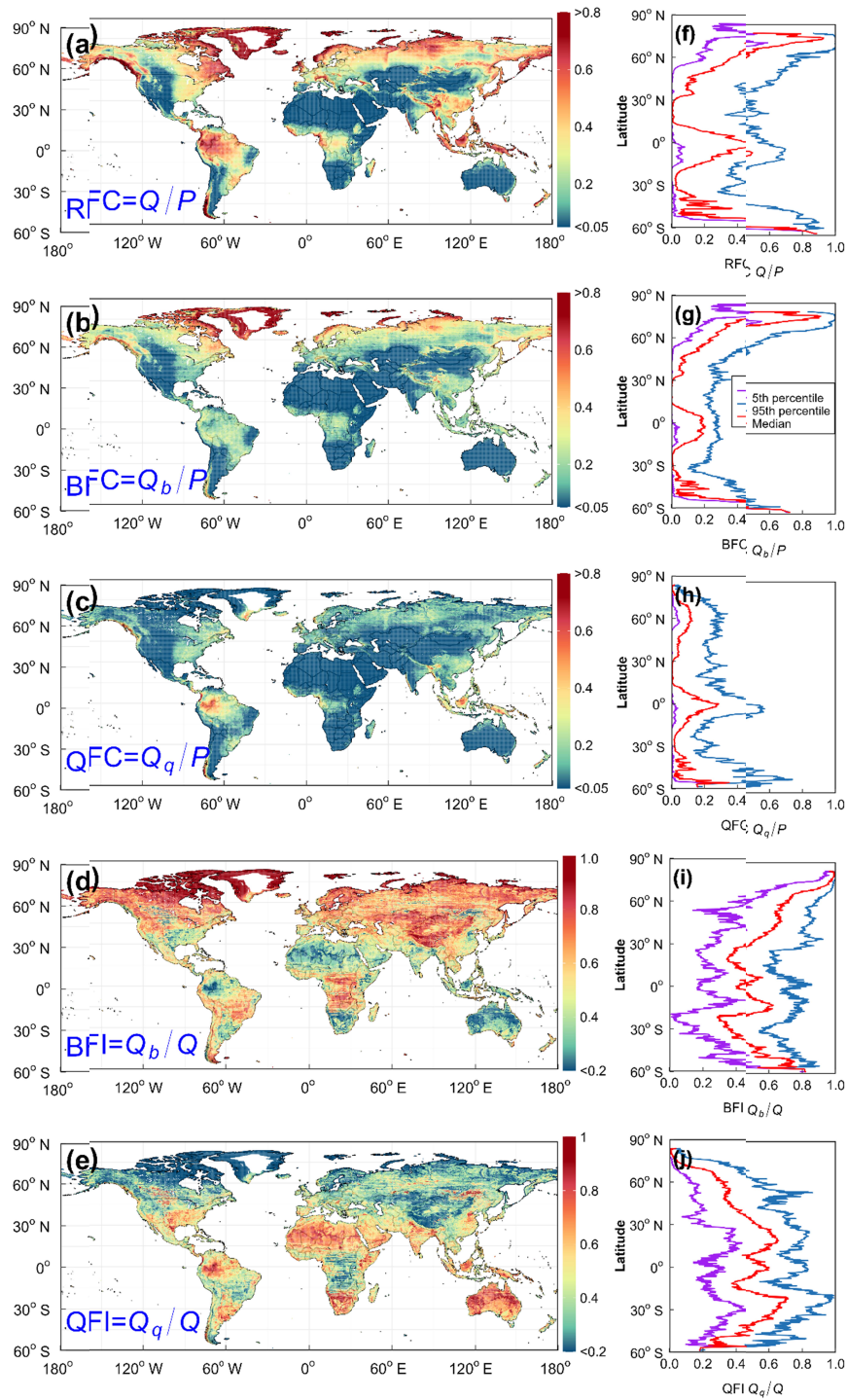
329

330 Figure 5. Global maps of estimated (a) Q , (c) Q_b and (e) Q_q . Station-based observed (b) Q , (d)
 331 Q_b and (f) Q_q .

332 Figure 6 shows the global map of gridded RFC, BFC, QFC, baseflow index
 333 (BFI= Q_b/Q) and quickflow index (QFI= Q_q/Q). RFC, BFC and QFC have similar
 334 spatial patterns with low values in western America, northern Africa, southern Africa,
 335 western Asia, central Asia, and Australia. However, regions with high RFC values,
 336 show both high and low BFC and QFC values depending on the region. For example,
 337 Q is partitioned more into Q_q than Q_b in the Amazon and southeast Asia, while in
 338 Canada and Russia, more Q_b is generated than Q_q . This is also illustrated with Figure
 339 6f–h, which show RFC, BFC and QFC for different quantiles as a function of the
 340 latitude. High RFC values are generally located at 60°N–85°N, 5°N–5°S and 45°S–
 341 60°S. In these latitudinal intervals, the partitioning of Q into Q_b and Q_q differs in
 342 space. As shown in Figure 6i and j, between 60°N–85°N, the majority of Q are mostly
 343 partitioned into Q_b (the median values in this latitudinal interval is on average 80.7%),
 344 and less Q_q (19.3%). Between 5°N–5°S and 45°S–60°S, the BFC and QFC are quite

345 similar to each other with Q_b of 42.1% and 54.9%, respectively, and Q_q of 57.9% and
346 45.1%, respectively. Across all latitudes, the mean difference between the 5th and 95th
347 quantiles is larger for RFC (0.50) and BFC (0.35) than for QFC (0.26). The spread of
348 QFC is more pronounced near the equator (5°N–5°S) and in the Southern
349 Hemisphere high latitudes (45°S–60°S). Overall, average 30.3% (std=26.5%) of P is
350 partitioned into Q , of which 20.6% (spatial standard deviation std=22.1%) is Q_b and
351 9.7% (std=10.3%) Q_q .

352



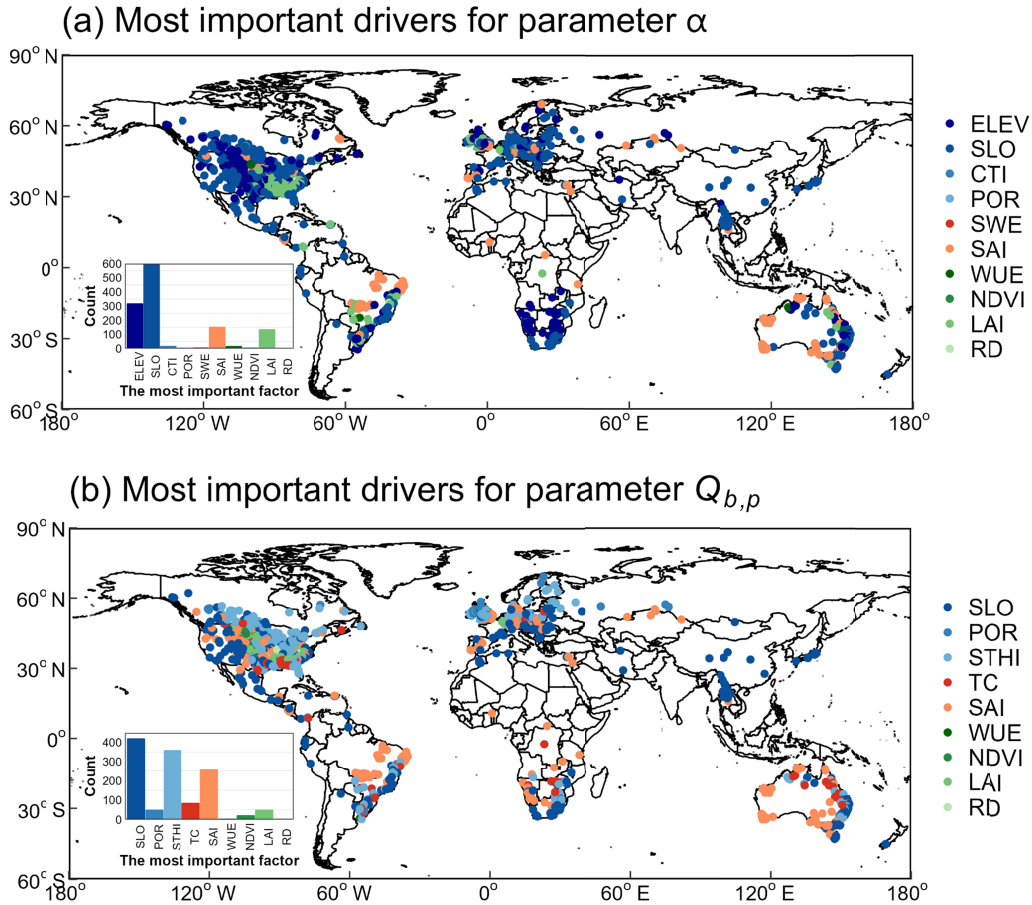
354

359 Figure 6. Global map of flow coefficients: (a) runoff coefficient (RFC) estimated with the
 360 Budyko curve (Eq. 3), (b) baseflow coefficient (BFC) estimated with the BFC curve (Eq. 4),
 361 (c) quickflow coefficient (QFC=RFC–BFC), (d) baseflow index (BFI= Q_b/Q) and (e)
 362 quickflow index (QFI= Q_q/Q). Subplots (f), (g), (h), (i) and (j) show the median latitudinal
 363 variation of the respective variables (in red), and the 5th (purple) and 95th (blue) percentiles.

359 **4.4 Dominant drivers of runoff partitioning**

360 The most important drivers for α and $Q_{b,p}$ vary across regions (Figure 7).
361 Topography and soil properties are most important for most catchments (75.5%
362 catchments for α ; 67.0% catchments for $Q_{b,p}$, see blue points in Figure 7). Slope (SLO)
363 is identified most frequently as the dominant driver for both α (48.7% catchments)
364 and $Q_{b,p}$ (34.1% catchments). The second driver is elevation (ELEV) for α dominant
365 in 25.6% catchments, and soil thickness (STHI) for $Q_{b,p}$ in 29.1% catchments.
366 Climate related factors are recognized as the most important driver at a smaller
367 number of catchments (12.4% for α and 27.3% for $Q_{b,p}$) as also vegetation related
368 factors (12.1% for α and 5.7% for $Q_{b,p}$).

369 The main drivers for the parameters are region specific. This provides another
370 perspective on why there is no universally accepted relationship yet (Padrón et al.,
371 2017), besides the complex interaction between the drivers (Ning et al., 2019) and
372 uncertainties in P , E_p , and Q (Koppa et al., 2021). Previous studies have investigated
373 the main drivers to Budyko parameters. These identified dominant drivers depend on
374 the region of interest and are different from each other. Considering large basins
375 globally, studies illustrated the main dominant property is vegetation (Li et al., 2013;
376 Zhang et al., 2001) or climate seasonality (Liu et al., 2018). In small catchments
377 regionally, the influence of climatic and physiographic properties on α becomes more
378 variable as other factors need to be considered including soil properties (Shen et al.,
379 2017), topography (Shao et al., 2012), human activities (Xing et al., 2018) and a
380 combination of various controls (Yang et al., 2007). According to the regions
381 identified in Figure 7, topography and soil related factors should be first considered
382 for regionalizing α in most catchments. Climate related factors are important in
383 eastern South America and the coastline of Australia. Vegetation is the most dominant
384 driver in western America and the United Kingdom.



386

389 Figure 7. Spatial distribution of the most important driver to: (a) parameter α in Budyko and
 390 BFC curves, and (b) parameter $Q_{b,p}$ in BFC curve. The explanation of the abbreviations is
 391 provided in Table 1.

390

391 5 Discussion

392 5.1 Comparison to existing global datasets

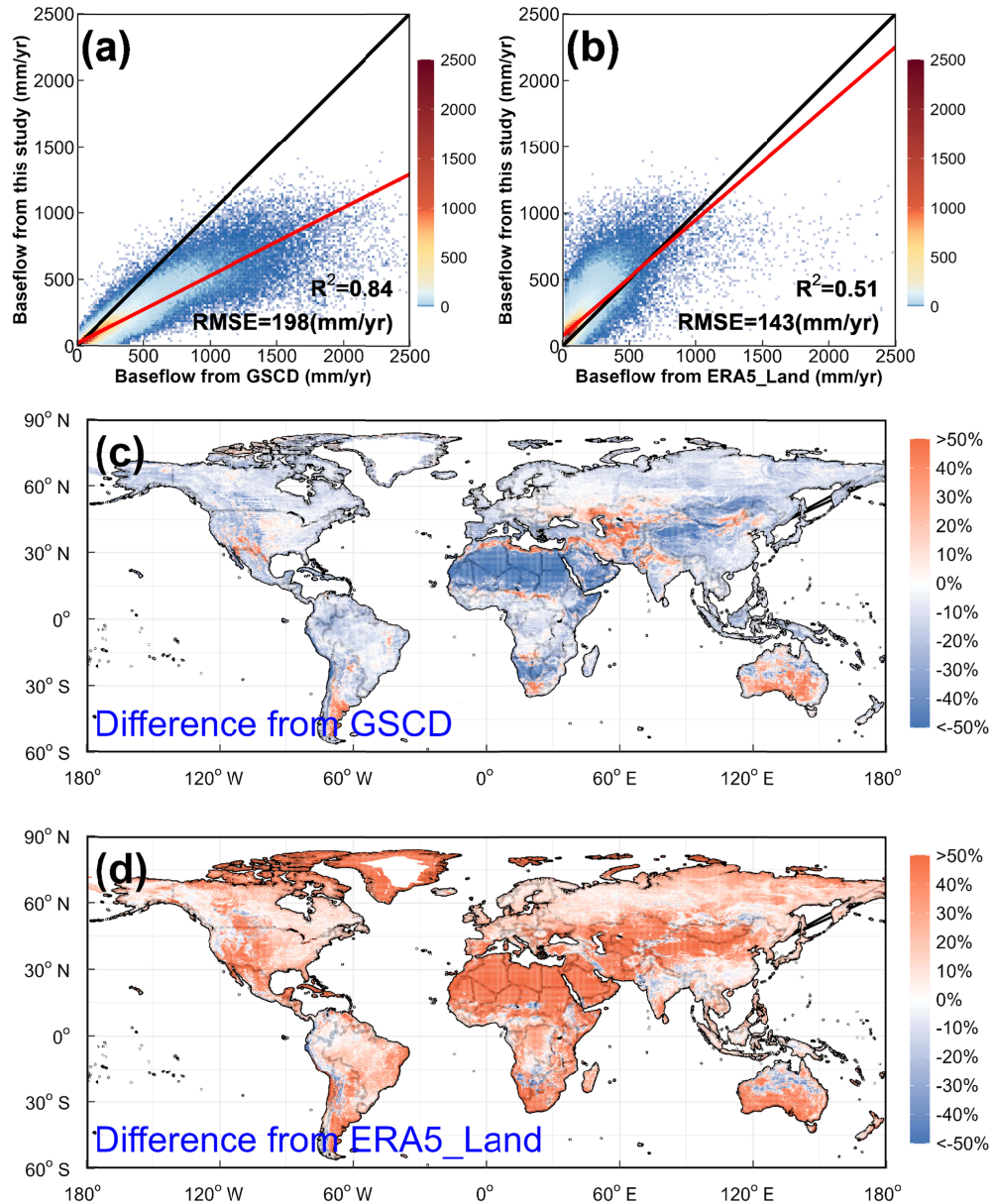
399 The global, gridded baseflow dataset developed in this study is compared to
 400 baseflow products from previous studies. This includes the Global Streamflow
 401 Characteristics Dataset (GSCD) (Beck et al., 2015) and ERA5-Land dataset (Muñoz
 402 Sabater, 2019). The baseflow is directly available in the ERA5-Land dataset, and
 403 indirectly with GSDC as only the baseflow index (BFI) and runoff (Q_{mean}) are
 404 provided. To remain consistent with this study, “BFI1” in the GSCD dataset is
 405 selected where the baseflow is also calculated from the digital filter method. The

399 long-term mean baseflow of this study (151 (spatial standard deviation std=181) mm
400 yr⁻¹) is smaller than GSCD-based baseflow ($Q_{b,GSCD} = 241$ (std=321) mm yr⁻¹, Figure
401 8a and c), and larger than ERA5-Land-based baseflow ($Q_{b,ERA5-Land} = 79$ (std=145)
402 mm yr⁻¹, Figure 8b and d). The baseflow estimated in this study has a larger spatial
403 correlation with $Q_{b,GSCD}$ ($R^2=0.84$) than $Q_{b,ERA5-Land}$ ($R^2=0.51$), while a smaller RMSE
404 is found relative to $Q_{b,ERA5-Land}$ (RMSE=143 mm yr⁻¹) compared to $Q_{b,GSCD}$
405 (RMSE=198 mm yr⁻¹). This means the spatial variability of our Budyko-ML-based
406 baseflow is more similar to GSCD, while the magnitudes are closer to ERA5-Land
407 values. The baseflow coefficient (BFC= Q_b/P) is also compared to estimates according
408 to GSCD and ERA5-Land. [Figure S4](#) shows that the correlation of BFC is higher
409 relative to GSCD ($R^2=0.73$) than ERA5-Land ($R^2=0.07$).

410 These three datasets are a result of different types of methods with each their
411 strengths and weaknesses: physically constrained ML in this study, pure ML for
412 GSCD and the land surface model H-TESSSEL for ERA5_Land. The GSCD dataset is
413 not physically constrained, but available at a higher spatial resolution (0.05°) and
414 based on significantly more catchments (3394). The H-TESSSEL used for ERA5_Land
415 is not specifically developed for runoff estimation, but for land-atmosphere
416 interactions. Also, H-TESSSEL uses “expert opinion” based parameterization instead
417 of being calibrated. This may be the cause for the poor correlation results and
418 confirms opinions that land surface models such as the H-TESSSEL poorly estimate
419 baseflow and groundwater-surface water interactions (Clark et al., 2015, Beck et al.,
420 2017).

421 As the baseflow index (BFI= Q_b/Q) is more sensitive to both baseflow and runoff
422 uncertainties (Gnann et al., 2019), the BFI is only compared to GSCD. As shown in
423 [Figure S5](#), the performance of BFI at catchment scale is acceptable with R^2 of 0.54.
424 However, the performance decreases at global grid scale ($R^2=0.18$). This low
425 correlation of BFI may be attributed to several aspects. First, getting accurate BFI
426 estimates from separately estimated Q and Q_b is difficult (Beck et al., 2017). The
427 spatial variability of the individual variables Q and Q_b is much larger than the
428 difference between Q and Q_b within each catchment (BFI). High similarities in the
429 spatial distribution of Q and Q_b does not guarantee similar BFI values. The BFI is
430 especially sensitive in dry regions since very low Q values (in the denominator)
431 would result in high BFI values. Second, the study period of the GSCD dataset and

437 this study is different. The GSCD dataset adopted average P and E_p datasets with
 438 daily Q datasets, while we kept their period consistent by selecting the crossing period.
 439 Third, the different digital filters used, Lyne–Hollick in this study and method from
 440 Van Dijk (2010) for GSCD, may cause a slight difference in the observed baseflow
 441 used to train models.



438
 442 Figure 8. Estimated global baseflow compared to GSCD (a and c) and ERA5-Land (b and d).
 443 Subplots (a) and (d) show the pixel-by-pixel scatter plot with the red lines representing the
 444 fitted curve, and the black lines the 1:1 line. Subplots (c) and (d) show the spatial distribution
 445 of their difference, calculated as their difference divide by their average (i.e., $(Q_{b,this\ study} -$

442 $Q_{b,GSCD}/(0.5 * (Q_{b,this\ study} + Q_{b,GSCD}))$ for plot (c), and replace $Q_{b,GSCD}$ with $Q_{b,ERA5-Land}$ for
443 plot (d).

444 **5.2 Partitioning in northern latitudes**

445 The runoff partitioning dataset developed in this study has difficulties in
446 representing high northern latitudes correctly (HNL). First, precipitation datasets tend
447 to be underestimated at latitudes higher than 60 °N (snow-dominant regions) at a
448 long-term scale (Beck et al., 2017). The MSWEP dataset used in this study attempted
449 to correct this underestimation bias by the catch-ratio equation (Goodison et al., 1998).
450 But the precipitation in HNL still has uncertainties for the gauge under-catch. By
451 using the Budyko constrained ML framework, precipitation is a dominant forcing for
452 the runoff and baseflow estimation, such that the uncertainty of precipitation could
453 bring large uncertainties. Second, there are no catchments in HNL when applying the
454 selection criteria as described in Section 3.1, which means relations based on trained
455 ML models may not be accurate there. As a data-oriented method, ML relies on
456 training data sources with all representative data expected to be included (Ma et al.,
457 2020). Third, the partitioning of baseflow and quickflow from snow-melt runoff is
458 different from precipitation-generated runoff. Based on the definition of baseflow
459 from Hall (1968), snow-melt runoff is grouped under baseflow. However, this
460 contradicts the digital filter technique that considers high frequency parts as
461 quickflow. Snow-melt runoff can have quickflow features of high frequency and
462 peaks during summer, even generating floods (Benn et al., 2012). As shown in Figure
463 6d and 6i, the baseflow index in high northern latitudes have high values, which
464 means runoff comes more from baseflow rather than quickflow. It makes sense if we
465 consider snow-melt runoff as baseflow following the definition of Hall (1968).
466 However, we recommend further investigation on runoff partitioning in NHL regions.

467 **6 Conclusion**

468 This study extends the Budyko constrained machine learning (Budyko–ML)
469 approach to develop global datasets for the runoff (Q), baseflow (Q_b), quickflow (Q_q)
470 and the respective coefficients relative to the precipitation (Q/P , Q_b/P and Q_q/P) at
471 0.25° resolution. This hybrid approach, combining the Budyko-based framework
472 (Budyko and BFC curve) with ML (BRT), retains the advantage of both the physical
473 part and ML to achieve good performances within physical boundaries. This

474 advantage is illustrated by the good performance of both Q and Q_b as they performed
475 well compared to field observations during the testing phase with $R^2=0.96$ and
476 $R^2=0.88$ for Q and Q_b , respectively. BRT estimates parameters globally, despite their
477 unknown relationship with climatic and physiographic properties. Among the 13
478 climatic and physiographic properties considered, the main drivers are region specific,
479 with topography and soil related factors being predominant in most catchments.
480 Findings indicate that global runoff amounts to 274 (spatial standard deviation
481 $\text{std}=418$) mm yr^{-1} , which means 30.3% ($\text{std}=26.5\%$) of the precipitation, of which
482 20.6 ($\text{std}=22.1\%$) is baseflow and 9.7% ($\text{std}=10.3\%$) is quickflow. Our baseflow
483 estimates are lower than GSCD estimates (241 ($\text{std}=321$) mm yr^{-1}) but larger than
484 ERA5-Land estimates (79 ($\text{std}=145$) mm yr^{-1}). These large differences illustrate the
485 large uncertainty that remains in runoff partitioning at global scales, and the required
486 efforts to improve it further.

487

488 **Data Availability Statement**

489 The developed global 0.25° datasets including runoff (Q), baseflow (Q_b), runoff
490 coefficient (Q/P), baseflow coefficient (Q_b/P) and baseflow index (Q_b/Q) are
491 available at [Global runoff partitioning based on Budyko-constrained machine learning](#)
492 [| Zenodo](#).

493

- 494 Abatzoglou, J. T., Dobrowski, S. Z., Parks, S. A., & Hegewisch, K. C. (2018).
496 TerraClimate, a high-resolution global dataset of monthly climate and climatic water
497 balance from 1958–2015. *Scientific Data* 2018 5:1, 5(1), 1–12.
498 <https://doi.org/10.1038/sdata.2017.191>
- 499 Amatulli, G., Domisch, S., Tuanmu, M. N., Parmentier, B., Ranipeta, A., Malczyk, J., &
500 Jetz, W. (2018). Data Descriptor: A suite of global, cross-scale topographic variables
501 for environmental and biodiversity modeling. *Scientific Data*, 5.
502 <https://doi.org/10.1038/sdata.2018.40>
- 503 Apurv, T., & Cai, X. (2020). Impact of Droughts on Water Supply in U.S. Watersheds:
504 The Role of Renewable Surface and Groundwater Resources. *Earth's Future*, 8(10).
505 <https://doi.org/10.1029/2020EF001648>
- 506 Bai, P., Liu, X., Zhang, D., & Liu, C. (2020). Estimation of the Budyko model parameter
507 for small basins in China. *Hydrological Processes*, 34(1), 125–138.
508 <https://doi.org/10.1002/hyp.13577>
- 509 Beck, H. E., van Dijk, A. I. J. M., Miralles, D. G., de Jeu, R. A. M., Bruijnzeel, L. A.,
510 McVicar, T. R., & Schellekens, J. (2013). Global patterns in base flow index and
511 recession based on streamflow observations from 3394 catchments. *Water Resources*
512 *Research*, 49(12), 7843–7863. <https://doi.org/10.1002/2013WR013918>
- 513 Beck, H. E., de Roo, A., & van Dijk, A. I. J. M. (2015). Global maps of streamflow
514 characteristics based on observations from several thousand catchments. *Journal of*
515 *Hydrometeorology*, 16(4), 1478–1501. <https://doi.org/10.1175/JHM-D-14-0155>.
- 516 Beck, H. E., Van Dijk, A. I. J. M., De Roo, A., Dutra, E., Fink, G., Orth, R., & Schellekens,
517 J. (2017). Global evaluation of runoff from 10 state-of-the-art hydrological models.
518 *Hydrology and Earth System Sciences*, 21(6), 2881–2903.
519 <https://doi.org/10.5194/hess-21-2881-2017>
- 520 Beck, H. E., Van Dijk, A. I. J. M., Levizzani, V., Schellekens, J., Miralles, D. G., Martens,
521 B., & De Roo, A. (2017). MSWEP: 3-hourly 0.25° global gridded precipitation
522 (1979–2015) by merging gauge, satellite, and reanalysis data. *Hydrology and Earth*
523 *System Sciences*, 21(1), 589–615. <https://doi.org/10.5194/HESS-21-589-2017>

52 Beck, H. E., Vergopolan, N., Pan, M., Levizzani, V., Van Dijk, A. I. J. M., Weedon, G. P.,
525 Brocca, L., Pappenberger, F., Huffman, G. J., & Wood, E. F. (2017). Global-scale
526 evaluation of 22 precipitation datasets using gauge observations and hydrological
527 modeling. *Hydrology and Earth System Sciences*, 21(12), 6201–6217.
528 <https://doi.org/10.5194/hess-21-6201-2017>

52 Benn, D. I., Bolch, T., Hands, K., Gulley, J., Luckman, A., Nicholson, L. I., Quincey, D.,
530 Thompson, S., Toumi, R., & Wiseman, S. (2012). Response of debris-covered
531 glaciers in the Mount Everest region to recent warming, and implications for outburst
532 flood hazards. In *Earth-Science Reviews* (Vol. 114, Issues 1–2, pp. 156–174).
533 <https://doi.org/10.1016/j.earscirev.2012.03.008>

53 Beven, K. J., & Kirkby, M. J. (1979). A physically based, variable contributing area model
535 of basin hydrology. *Hydrological Sciences Bulletin*, 24(1), 43–69.
536 <https://doi.org/10.1080/02626667909491834>

53 de Bézenac, E., Pajot, A., & Gallinari, P. (2019). Deep learning for physical processes:
538 incorporating prior scientific knowledge. *Journal of Statistical Mechanics: Theory
539 and Experiment*, 2019(12), 124009. <https://doi.org/10.1088/1742-5468/ab3195>

54 Budyko, M. I. (1961). The Heat Balance of the Earth's Surface. *Soviet Geography*, 2(4), 3–
541 13. <https://doi.org/10.1080/00385417.1961.10770761>

54 Cheng, S., Cheng, L., Liu, P., Qin, S., Zhang, L., Xu, C. Y., et al. (2021). An Analytical
543 Baseflow Coefficient Curve for Depicting the Spatial Variability of Mean Annual
544 Catchment Baseflow. *Water Resources Research*, 57(8).
545 <https://doi.org/10.1029/2020WR029529>

54 Cheng, S., Cheng, L., Qin, S., Zhang, L., Liu, P., Liu, L., et al. (2022). Improved
547 Understanding of How Catchment Properties Control Hydrological Partitioning
548 Through Machine Learning. *Water Resources Research*, 58(4).
549 <https://doi.org/10.1029/2021WR031412>

55 Choudhury, Bhaskar J. (1999). Evaluation of an empirical equation for annual evaporation
551 using field observations and results from a biophysical model. *Journal of Hydrology*,
552 216(1), 99–110. [https://doi.org/https://doi.org/10.1016/S0022-1694\(98\)00293-5](https://doi.org/https://doi.org/10.1016/S0022-1694(98)00293-5)

55 Clark, M. P., Fan, Y., Lawrence, D. M., Adam, J. C., Bolster, D., Gochis, D. J., et al.
554 (2015). Improving the representation of hydrologic processes in Earth System Models.

555 *Water Resources Research*, 51(8), 5929–5956.
556 <https://doi.org/10.1002/2015WR017096>

557 van Dijk, A. I. J. M. (2010). Climate and terrain factors explaining streamflow response
558 and recession in Australian catchments. *Hydrology and Earth System Sciences*, 14(1),
559 159–169. <https://doi.org/10.5194/HESS-14-159-2010>

560 Elith, J., Leathwick, J. R., & Hastie, T. (2008). A working guide to boosted regression
561 trees. *Journal of Animal Ecology*. <https://doi.org/10.1111/j.1365-2656.2008.01390.x>

562 Sanderson Eric W., Malanding Jaiteh, Marc A. Levy, Kent H. Redford, Antoinette V.
563 Wannebo, & Gillian Woolmer. (2002). The Human Footprint and the Last of the Wild.
564 *BioScience*, 52(10), 891–904.

565 Fan, Y., Miguez-Macho, G., Jobbágy, E. G., Jackson, R. B., & Otero-Casal, C. (2017).
566 Hydrologic regulation of plant rooting depth. *Proceedings of the National Academy of*
567 *Sciences of the United States of America*, 114(40), 10572–10577.
568 <https://doi.org/10.1073/pnas.1712381114>

569 Franklin, J. (2008). The elements of statistical learning: data mining, inference and
570 prediction. *The Mathematical Intelligencer* 2005 27:2, 27(2), 83–85.
571 <https://doi.org/10.1007/BF02985802>

572 Eu, B. F. (1981). On the calculation of the evaporation from land surface. *Chinese Journal*
573 *of Atmospheric Sciences*, 5(1), 23–31.

574 Gnann, S. J., Woods, R. A., & Howden, N. J. K. (2019). Is There a Baseflow Budyko
575 Curve? *Water Resources Research*, 55(4), 2838–2855.
576 <https://doi.org/10.1029/2018WR024464>

577 Good, S. P., Moore, G. W., & Miralles, D. G. (2017). A mesic maximum in biological
578 water use demarcates biome sensitivity to aridity shifts. *Nature Ecology and*
579 *Evolution*, 1(12), 1883–1888. <https://doi.org/10.1038/s41559-017-0371-8>

580 Goodison, B., Louie, P., & Yang, D. (1998). WMO Solid Precipitation Measurement
581 Intercomparison. *World Meteorological Organization-Publications-WMO TD*, 67.

582 Hall, F. R. (1968). Base-Flow Recessions—A Review. *Water Resources Research*, 4(5),
583 973–983. <https://doi.org/10.1029/WR004I005P00973>

584 Hirsbach, H., Bell, B., Berrisford, P., Hirahara, S., Horányi, A., Muñoz-Sabater, J.,
585 Nicolas, J., Peubey, C., Radu, R., Schepers, D., Simmons, A., Soci, C., Abdalla, S.,
586 Abellan, X., Balsamo, G., Bechtold, P., Biavati, G., Bidlot, J., Bonavita, M., ...
587 Thépaut, J. N. (2020). The ERA5 global reanalysis. *Quarterly Journal of the Royal*
588 *Meteorological Society*, 146(730), 1999–2049. <https://doi.org/10.1002/qj.3803>

589 Huang, S., Dong, Q., Zhang, X., & Deng, W. (2021). Catchment natural driving factors
590 and prediction of baseflow index for Continental United States based on Random
591 Forest technique. *Stochastic Environmental Research and Risk Assessment*, 35(12),
592 2567–2581. <https://doi.org/10.1007/s00477-021-02057-2>

593 Jung, M., Reichstein, M., Ciais, P., Seneviratne, S. I., Sheffield, J., Goulden, M. L., Bonan,
594 G., Cescatti, A., Chen, J., De Jeu, R., Dolman, A. J., Eugster, W., Gerten, D., Gianelle,
595 D., Gobron, N., Heinke, J., Kimball, J., Law, B. E., Montagnani, L., Zhang, K. (2010).
596 Recent decline in the global land evapotranspiration trend due to limited moisture
597 supply. *Nature*, 467(7318), 951–954. <https://doi.org/10.1038/nature09396>

598 Kraft, B., Jung, M., Körner, M., Koirala, S., & Reichstein, M. (2022). Towards hybrid
599 modeling of the global hydrological cycle. *Hydrology and Earth System Sciences*,
600 26(6), 1579–1614. <https://doi.org/10.5194/hess-26-1579-2022>

601 Koppa, A., Alam, S., Miralles, D. G., & Gebremichael, M. (2021). Budyko-Based Long-
602 Term Water and Energy Balance Closure in Global Watersheds From Earth
603 Observations. *Water Resources Research*, 57(5).
604 <https://doi.org/10.1029/2020WR028658>

605 Koppa, A., Rains, D., Hulsman, P., Poyatos, R., & Miralles, D. G. (2022). A deep learning-
606 based hybrid model of global terrestrial evaporation. *Nature Communications*, 13(1),
607 1912. <https://doi.org/10.1038/s41467-022-29543-7>

608 Li, D., Pan, M., Cong, Z., Zhang, L., & Wood, E. (2013). Vegetation control on water and
609 energy balance within the Budyko framework. *Water Resources Research*, 49(2),
610 969–976. <https://doi.org/10.1002/wrcr.20107>

611 Liu, J., & You, Y. (2021). The Roles of Catchment Characteristics in Precipitation
612 Partitioning Within the Budyko Framework. *Journal of Geophysical Research:*
613 *Atmospheres*, 126(16). <https://doi.org/10.1029/2021JD035168>

- 61 Liu, J., Zhang, Q., Singh, V. P., Song, C., Zhang, Y., Sun, P., & Gu, X. (2018).
615 Hydrological effects of climate variability and vegetation dynamics on annual fluvial
616 water balance in global large river basins. *Hydrology and Earth System Sciences*,
617 22(7), 4047–4060. <https://doi.org/10.5194/HESS-22-4047-2018>
- 618 Lyne, V., & Hollick, M. (1979). Stochastic time-variable rainfall-runoff modelling. In
619 *Institute of Engineers Australia National Conference*. Perth. Retrieved from
620 <https://www.academia.edu>
- 621 Ma, K., Feng, D., Lawson, K., Tsai, W. P., Liang, C., Huang, X., et al. (2021).
622 Transferring Hydrologic Data Across Continents – Leveraging Data-Rich Regions to
623 Improve Hydrologic Prediction in Data-Sparse Regions. *Water Resources Research*,
624 57(5). <https://doi.org/10.1029/2020WR028600>
- 625 Martens, B., Miralles, D. G., Lievens, H., van der Schalie, R., de Jeu, R. A. M., Fernández-
626 Prieto, D., et al. (2017). GLEAM v3: Satellite-based land evaporation and root-zone
627 soil moisture. *Geoscientific Model Development*, 10(5), 1903–1925.
628 <https://doi.org/10.5194/GMD-10-1903-2017>
- 629 Marthews, T. R., Dadson, S. J., Lehner, B., Abele, S., & Gedney, N. (2015). High-
630 resolution global topographic index values for use in large-scale hydrological
631 modelling. *Hydrology and Earth System Sciences*, 19(1), 91–104.
632 <https://doi.org/10.5194/hess-19-91-2015>
- 633 Mianabadi, A., Davary, K., Pourreza-Bilondi, M., & Coenders-Gerrits, A. M. J. (2020,
634 September 1). Budyko framework; towards non-steady state conditions. *Journal of*
635 *Hydrology*. Elsevier B.V. <https://doi.org/10.1016/j.jhydrol.2020.125089>
- 636 Miller, M. P., Buto, S. G., Susong, D. D., & Rumsey, C. A. (2016). The importance of base
637 flow in sustaining surface water flow in the Upper Colorado River Basin. *Water*
638 *Resources Research*, 52(5), 3547–3562. <https://doi.org/10.1002/2015WR017963>
- 639 Miralles, D. G., Holmes, T. R. H., de Jeu, R. A. M., Gash, J. H., Meesters, A. G. C. A., &
640 Dolman, A. J. (2011). Global land-surface evaporation estimated from satellite-based
641 observations. *Hydrology and Earth System Sciences*, 15(2), 453–469.
642 <https://doi.org/10.5194/hess-15-453-2011>
- 643 Muñoz-Sabater, J., Dutra, E., Agustí-Panareda, A., Albergel, C., Arduini, G., Balsamo, G.,
644 Boussetta, S., Choulga, M., Harrigan, S., Hersbach, H., Martens, B., Miralles, D. G.,

645 Piles, M., Rodríguez-Fernández, N. J., Zsoter, E., Buontempo, C., & Thépaut, J. N.
646 (2021). ERA5-Land: A state-of-the-art global reanalysis dataset for land applications.
647 *Earth System Science Data*, 13(9), 4349–4383. [https://doi.org/10.5194/essd-13-4349-](https://doi.org/10.5194/essd-13-4349-2021)
648 2021

649 Nathan, R. J., & McMahon, T. A. (1990). Evaluation of automated techniques for base
650 flow and recession analyses. *Water Resources Research*, 26(7), 1465–1473.
651 <https://doi.org/10.1029/WR026I007P01465>

652 Ding, T., Zhou, S., Chang, F., Shen, H., Li, Z., & Liu, W. (2019). Interaction of vegetation,
653 climate and topography on evapotranspiration modelling at different time scales
654 within the Budyko framework. *Agricultural and Forest Meteorology*, 275, 59–68.
655 <https://doi.org/10.1016/j.agrformet.2019.05.001>

656 Padrón, R. S., Gudmundsson, L., Greve, P., & Seneviratne, S. I. (2017). Large-Scale
657 Controls of the Surface Water Balance Over Land: Insights From a Systematic
658 Review and Meta-Analysis. *Water Resources Research*, 53(11), 9659–9678.
659 <https://doi.org/10.1002/2017WR021215>

660 Roggio, L., de Sousa, L. M., Batjes, N. H., Heuvelink, G. B. M., Kempen, B., Ribeiro, E.,
661 & Rossiter, D. (2021). SoilGrids 2.0: Producing soil information for the globe with
662 quantified spatial uncertainty. *SOIL*, 7(1), 217–240. [https://doi.org/10.5194/soil-7-](https://doi.org/10.5194/soil-7-217-2021)
663 [217-2021](https://doi.org/10.5194/soil-7-217-2021)

664 Porporato, A., Daly, E., & Rodriguez-Iturbe, I. (2004). Soil water balance and ecosystem
665 response to climate change. *American Naturalist*, 164(5), 625–632.
666 <https://doi.org/10.1086/424970/ASSET/IMAGES/LARGE/FG3.JPEG>

667 Potter, N. J., Zhang, L., D Milly, P. C., McMahon, T. A., & Jakeman, A. J. (2005). Effects
668 of rainfall seasonality and soil moisture capacity on mean annual water balance for
669 Australian catchments, 6007. <https://doi.org/10.1029/2004WR003697>

670 Ribeiro, M. T., Singh, S., & Guestrin, C. (2016). Why should I trust you, explaining the
671 predictions of any classifier. KDD 2016. <https://doi.org/10.1145/2939672.2939778>

672 Roxy, M. K., Ghosh, S., Pathak, A., Athulya, R., Mujumdar, M., Murtugudde, R., et al.
673 (2017). A threefold rise in widespread extreme rain events over central India. *Nature*
674 *Communications* 2017 8:1, 8(1), 1–11. <https://doi.org/10.1038/s41467-017-00744-9>

675 Sadeghi, M., Asanjan, A. A., Faridzad, M., Nguyen, P. H. U., Hsu, K., Sorooshian, S., &
676 Braithwaite, D. A. N. (2019). PERSIANN-CNN: Precipitation estimation from
677 remotely sensed information using artificial neural networks–convolutional neural
678 networks. *Journal of Hydrometeorology*, 20(12), 2273–2289.
679 <https://doi.org/10.1175/JHM-D-19-0110.1>

680 hao, Q., Traylen, A., & Zhang, L. (2012). Nonparametric method for estimating the
681 effects of climatic and catchment characteristics on mean annual evapotranspiration.
682 *Water Resources Research*, 48(3), 3517. <https://doi.org/10.1029/2010WR009610>

683 Shen, C. (2018). A Transdisciplinary Review of Deep Learning Research and Its
684 Relevance for Water Resources Scientists. *Water Resources Research*, 54(11), 8558–
685 8593. <https://doi.org/10.1029/2018WR022643>

686 Shen, Q., Cong, Z., & Lei, H. (2017). Evaluating the impact of climate and underlying
687 surface change on runoff within the Budyko framework: A study across 224
688 catchments in China. *Journal of Hydrology*, 554, 251–262.
689 <https://doi.org/10.1016/j.jhydrol.2017.09.023>

690 Tan, X., Liu, B., & Tan, X. (2020). Global Changes in Baseflow Under the Impacts of
691 Changing Climate and Vegetation. *Water Resources Research*, 56(9).
692 <https://doi.org/10.1029/2020WR027349>

693 Tang, Y., & Wang, D. (2017). Evaluating the role of watershed properties in long-term
694 water balance through a Budyko equation based on two-stage partitioning of
695 precipitation. *Water Resources Research*, 53(5), 4142–4157.
696 <https://doi.org/10.1002/2016WR019920>

697 Xie, K., Liu, P., Zhang, J., Han, D., Wang, G., & Shen, C. (2021). Physics-guided deep
698 learning for rainfall-runoff modeling by considering extreme events and monotonic
699 relationships. *Journal of Hydrology*, 603, 127043.
700 <https://doi.org/10.1016/J.JHYDROL.2021.127043>

701 King, W., Wang, W., Shao, Q., & Yong, B. (2018). Identification of dominant interactions
702 between climatic seasonality, catchment characteristics and agricultural activities on
703 Budyko-type equation parameter estimation. *Journal of Hydrology*, 556, 585–599.
704 <https://doi.org/10.1016/j.jhydrol.2017.11.048>

70 Yamazaki, D., Ikeshima, D., Sosa, J., Bates, P. D., Allen, G. H., & Pavelsky, T. M. (2019).
706 MERIT Hydro: A High-Resolution Global Hydrography Map Based on Latest
707 Topography Dataset. *Water Resources Research*, 55(6), 5053–5073.
708 <https://doi.org/10.1029/2019WR024873>

70 Yang, D., Sun, F., Liu, Z., Cong, Z., Ni, G., & Lei, Z. (2007). Analyzing spatial and
710 temporal variability of annual water-energy balance in nonhumid regions of China
711 using the Budyko hypothesis. *Water Resources Research*, 43(4).
712 <https://doi.org/10.1029/2006WR005224>

71 Yin, J., Gentile, P., Zhou, S., Sullivan, S. C., Wang, R., Zhang, Y., & Guo, S. (2018).
714 Large increase in global storm runoff extremes driven by climate and anthropogenic
715 changes. *Nature Communications*, 9(1). <https://doi.org/10.1038/s41467-018-06765-2>

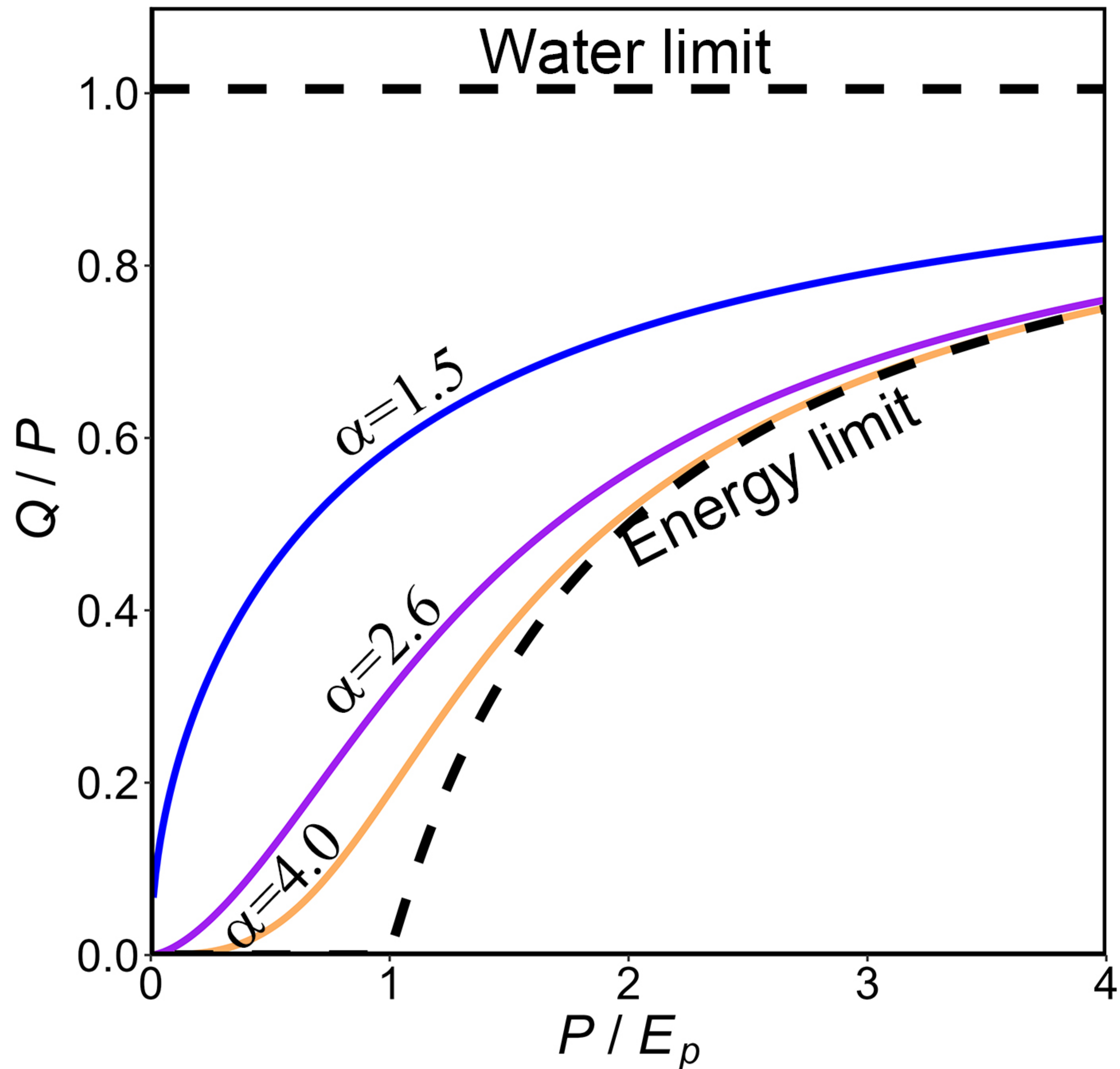
71 Zhang, L., Dawes, W. R., & Walker, G. R. (2001). Response of mean annual
717 evapotranspiration to vegetation changes at catchment scale. *Water Resources*
718 *Research*, 37(3), 701–708. <https://doi.org/10.1029/2000WR900325>

71 Zhang, L., Hickel, K., Dawes, W. R., Chiew, F. H. S., Western, A. W., & Briggs, P. R.
720 (2004). A rational function approach for estimating mean annual evapotranspiration.
721 *Water Resources Research*, 40(2). <https://doi.org/10.1029/2003WR002710>

72 Zhao, W. L., Gentile, P., Reichstein, M., Zhang, Y., Zhou, S., Wen, Y., Lin, C., Li, X., &
723 Qiu, G. Y. (2019). Physics-Constrained Machine Learning of Evapotranspiration.
724 *Geophysical Research Letters*, 46(24), 14496–14507.
725 <https://doi.org/10.1029/2019GL085291>

Figure1.

(a) Budyko framework



(b) BFC curve

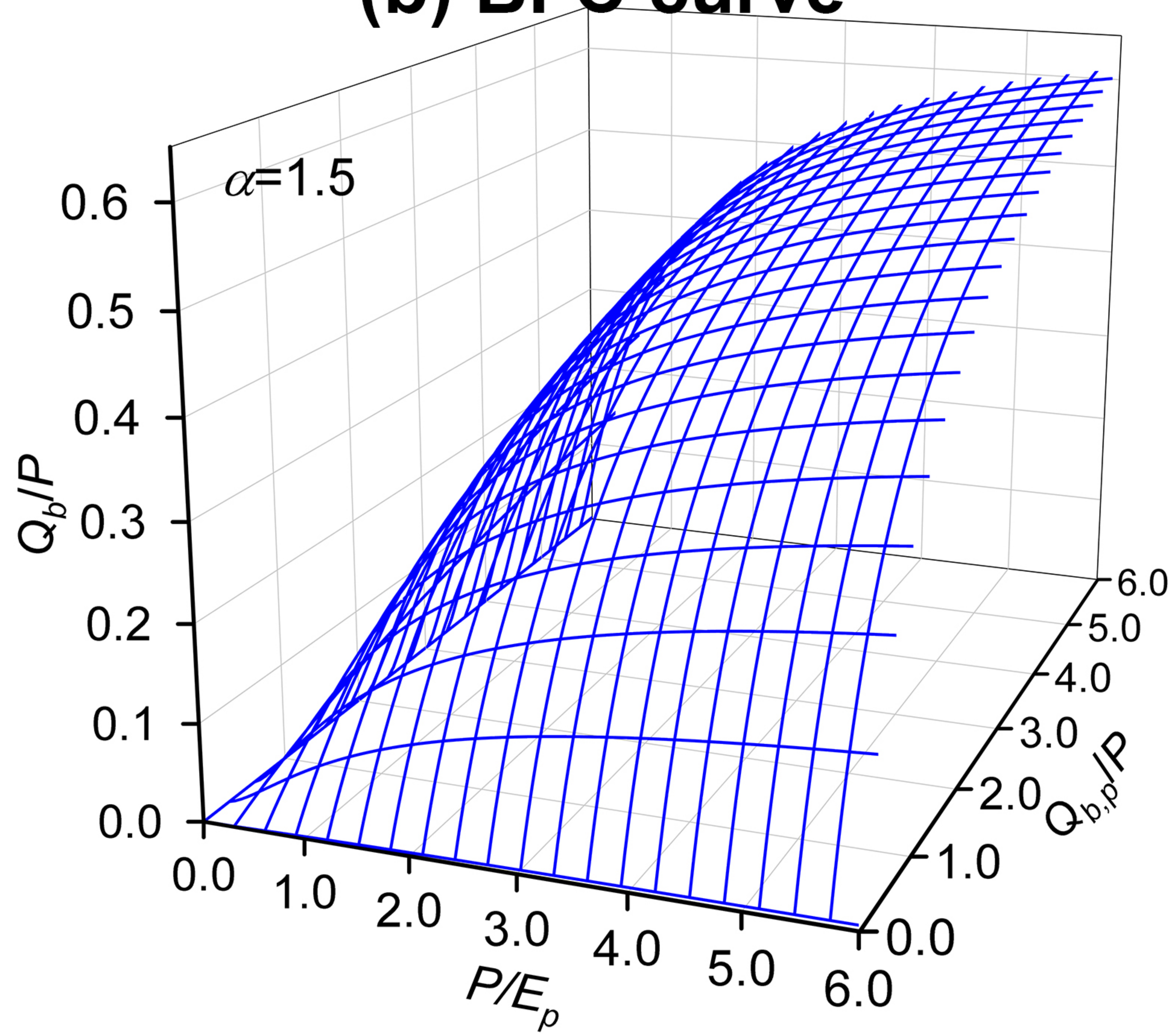
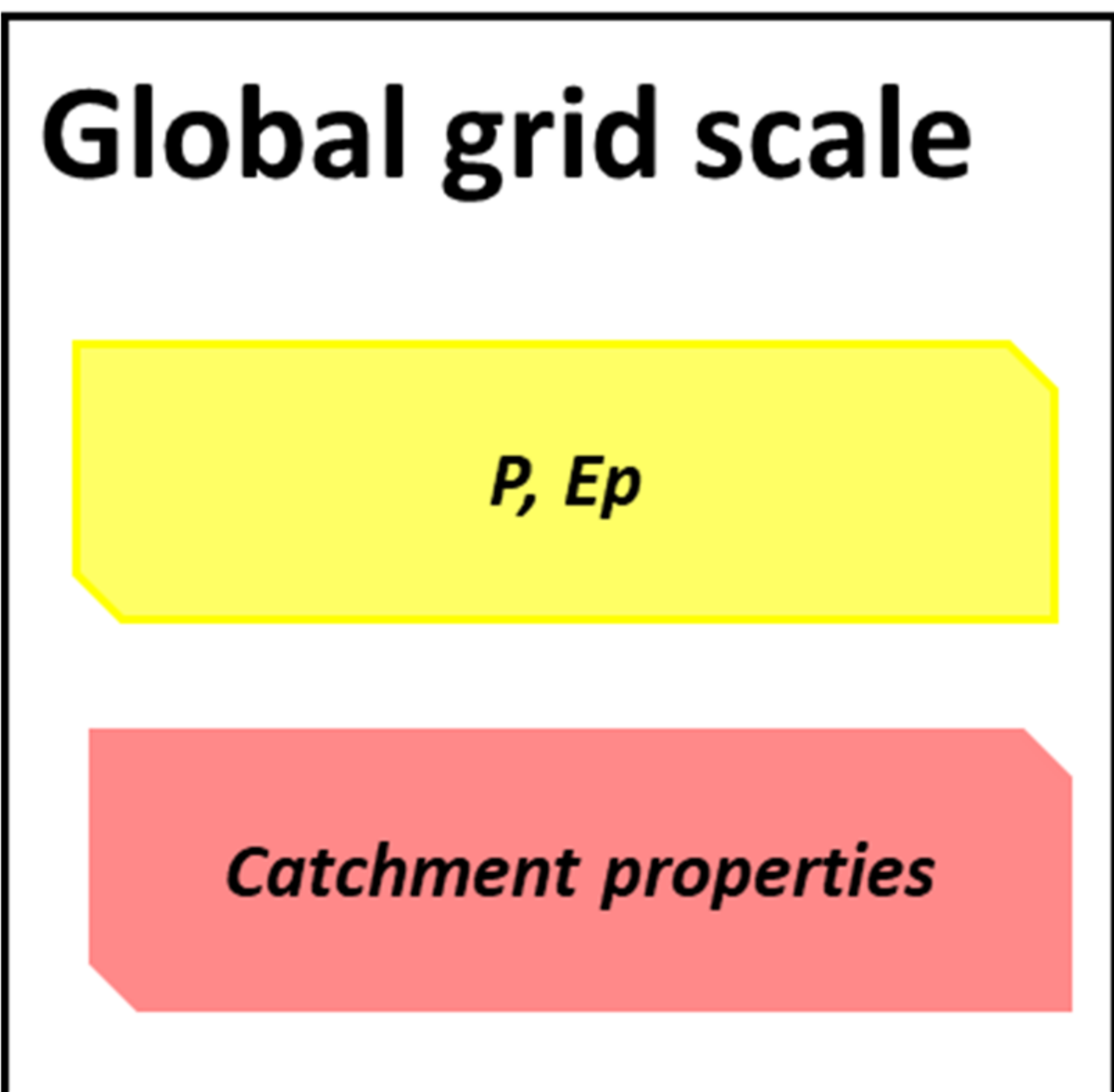
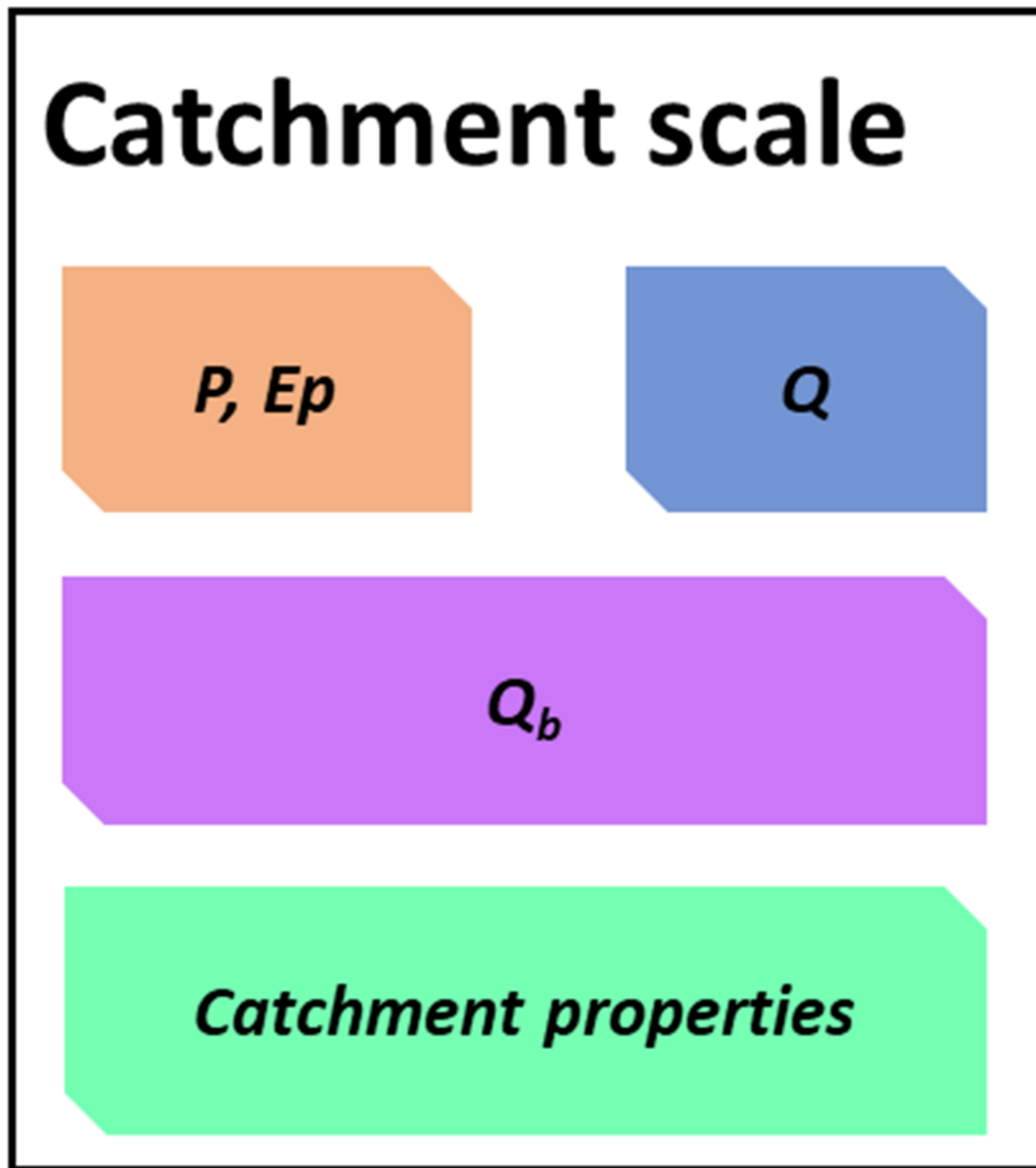


Figure2.

Input dataset



Method

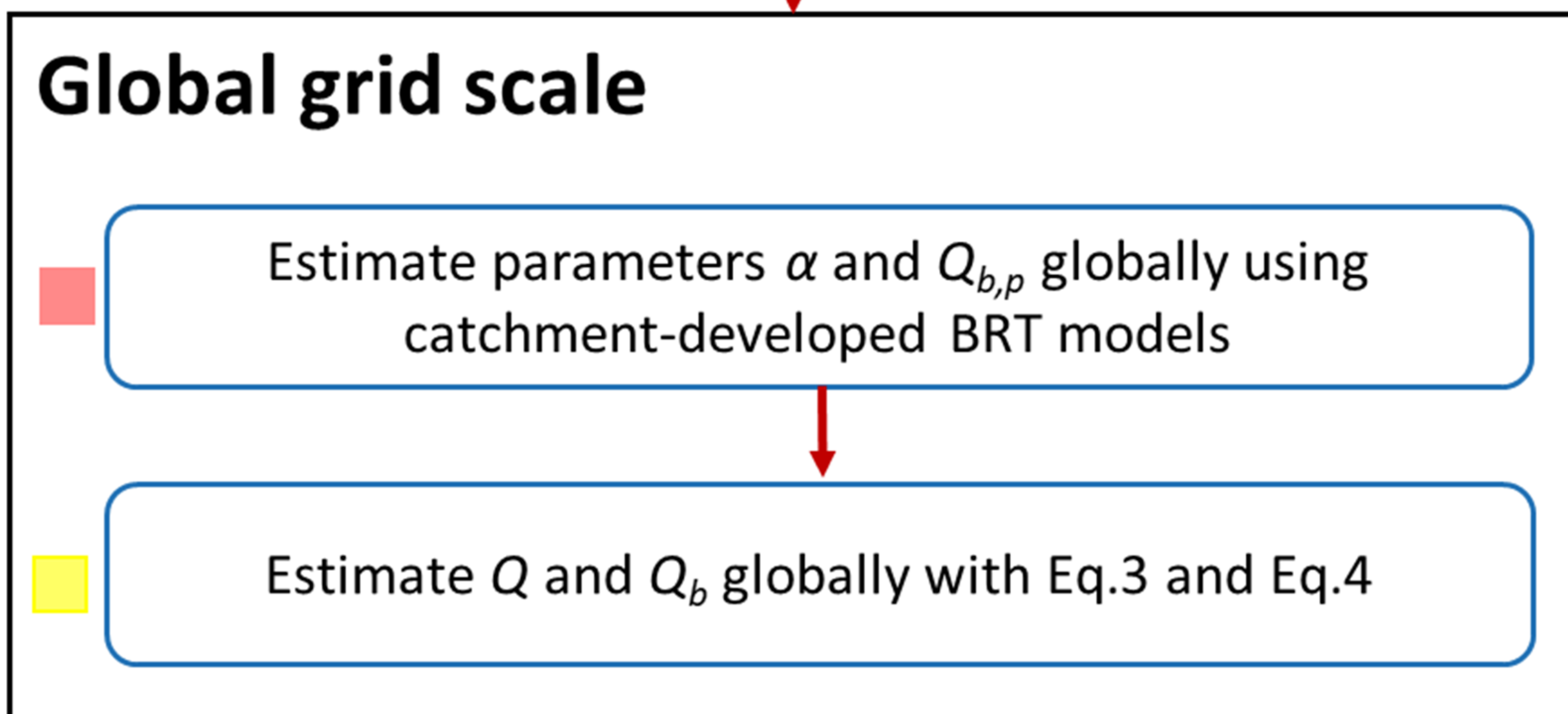
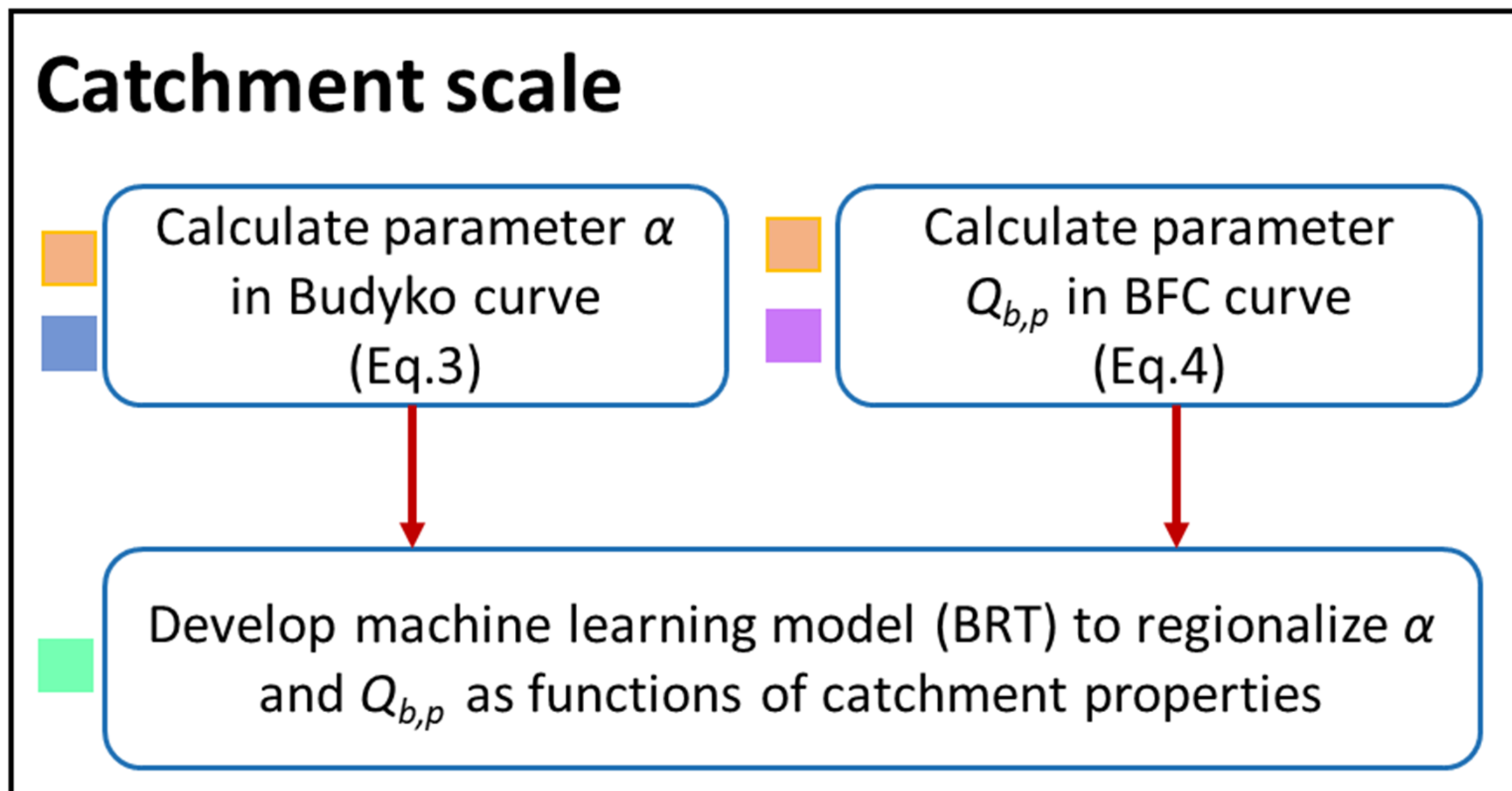


Figure3.

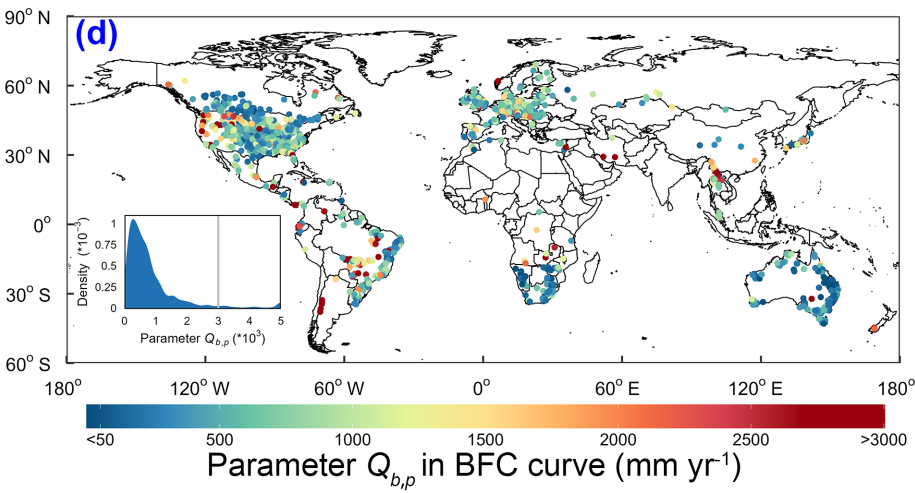
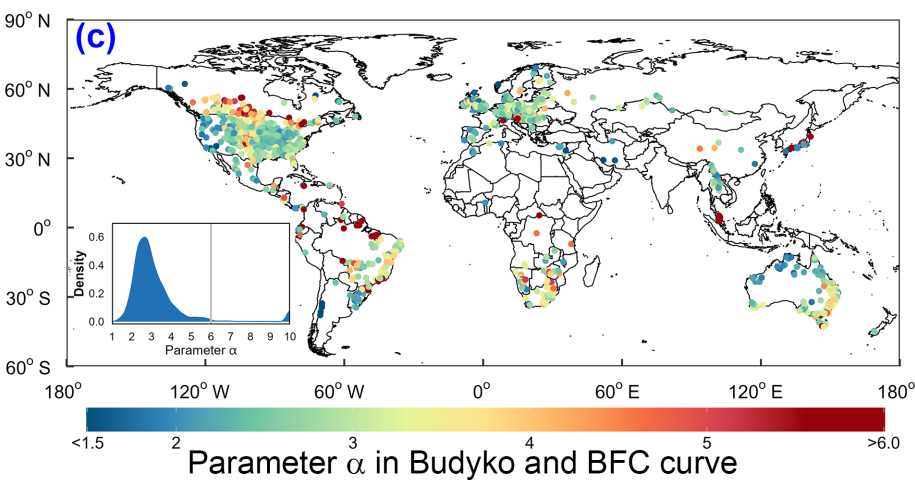
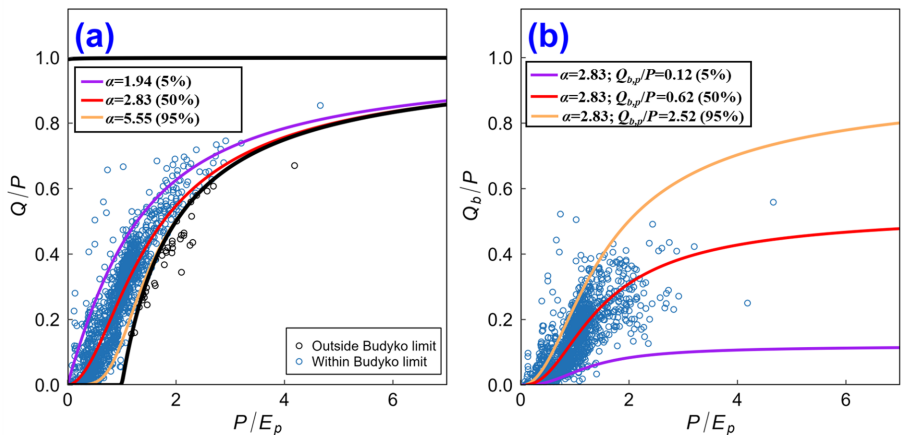


Figure4.

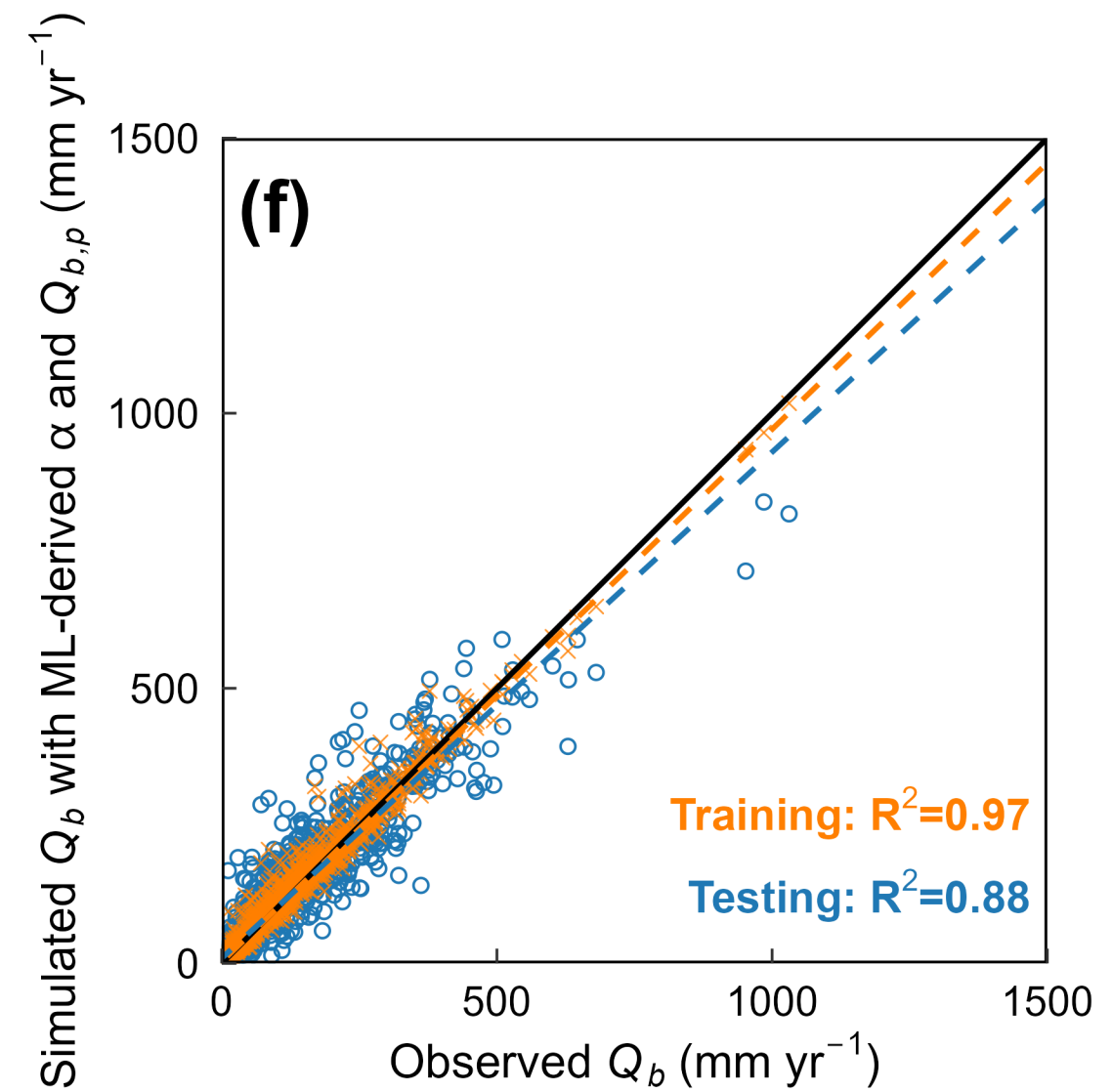
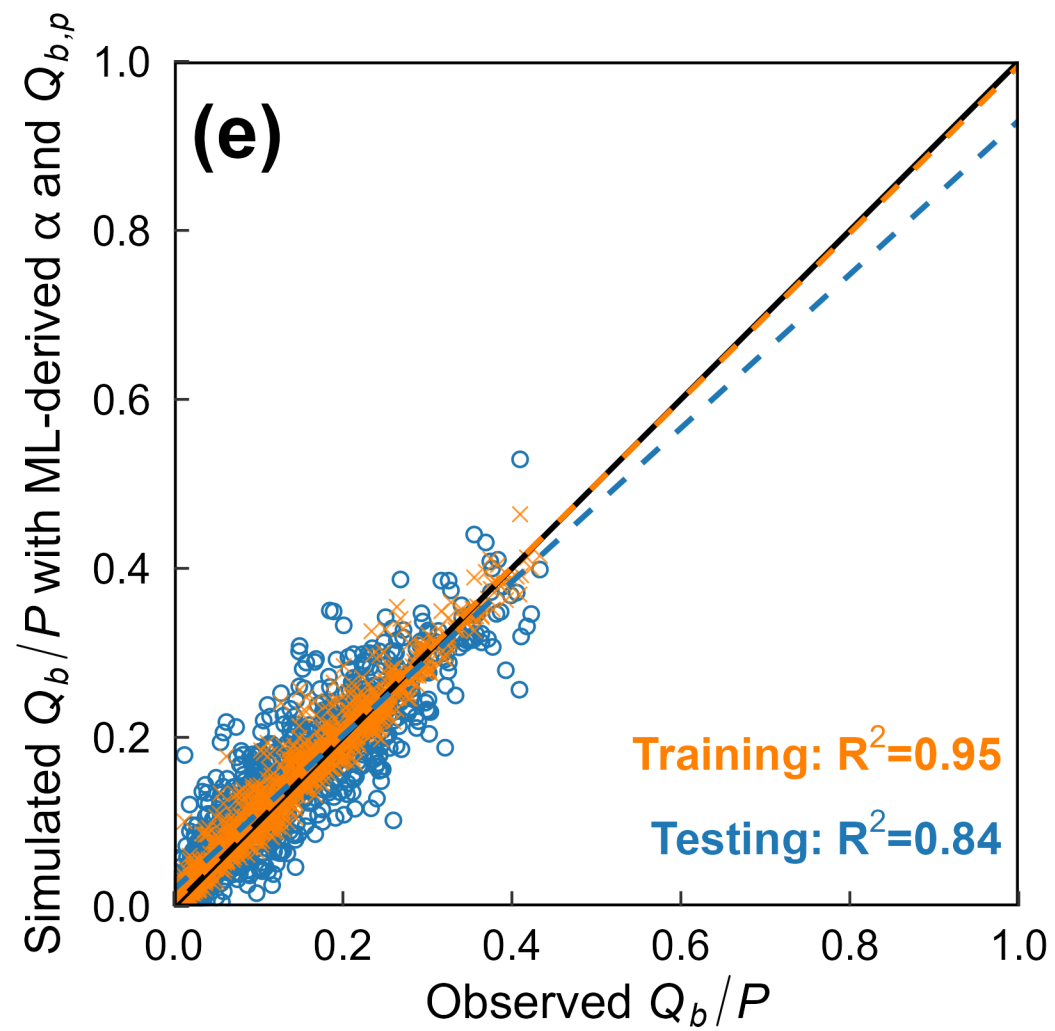
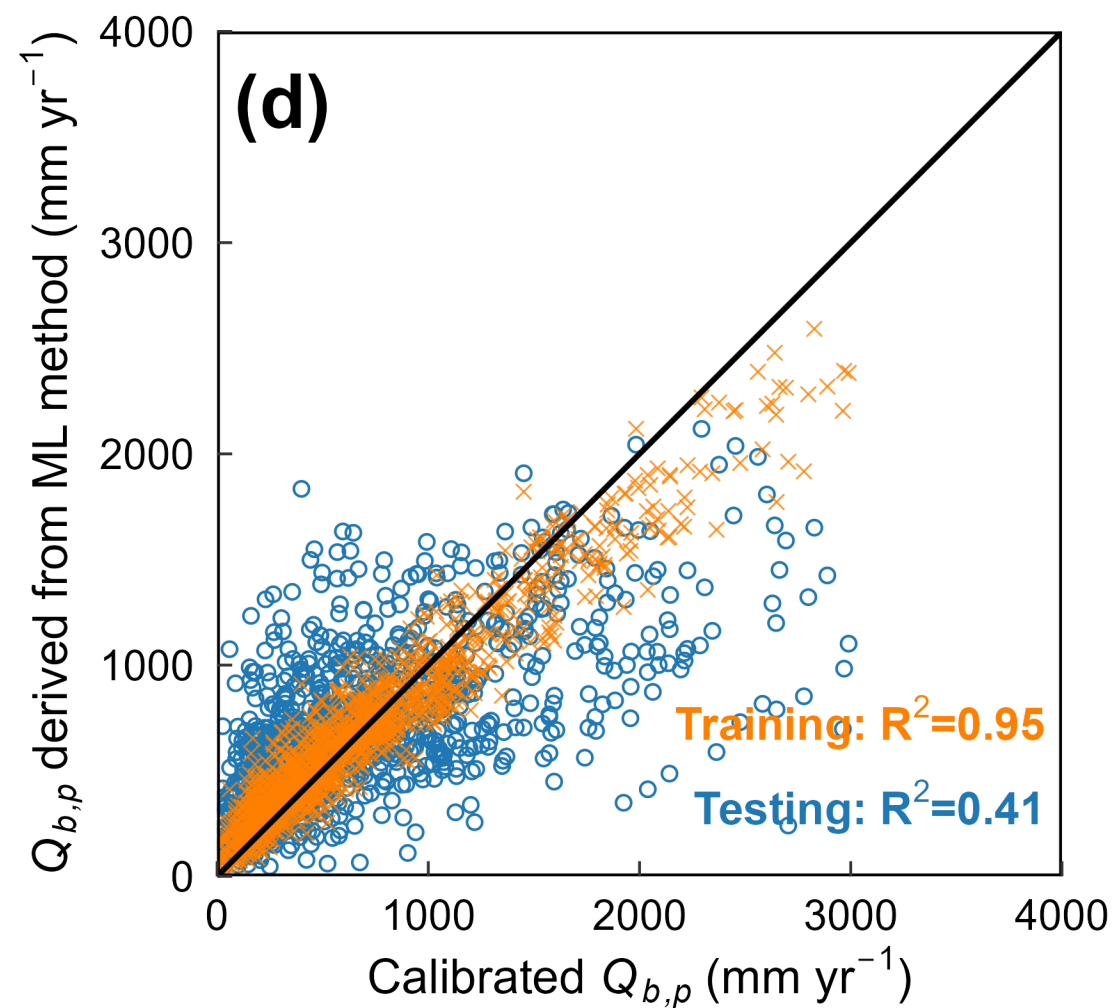
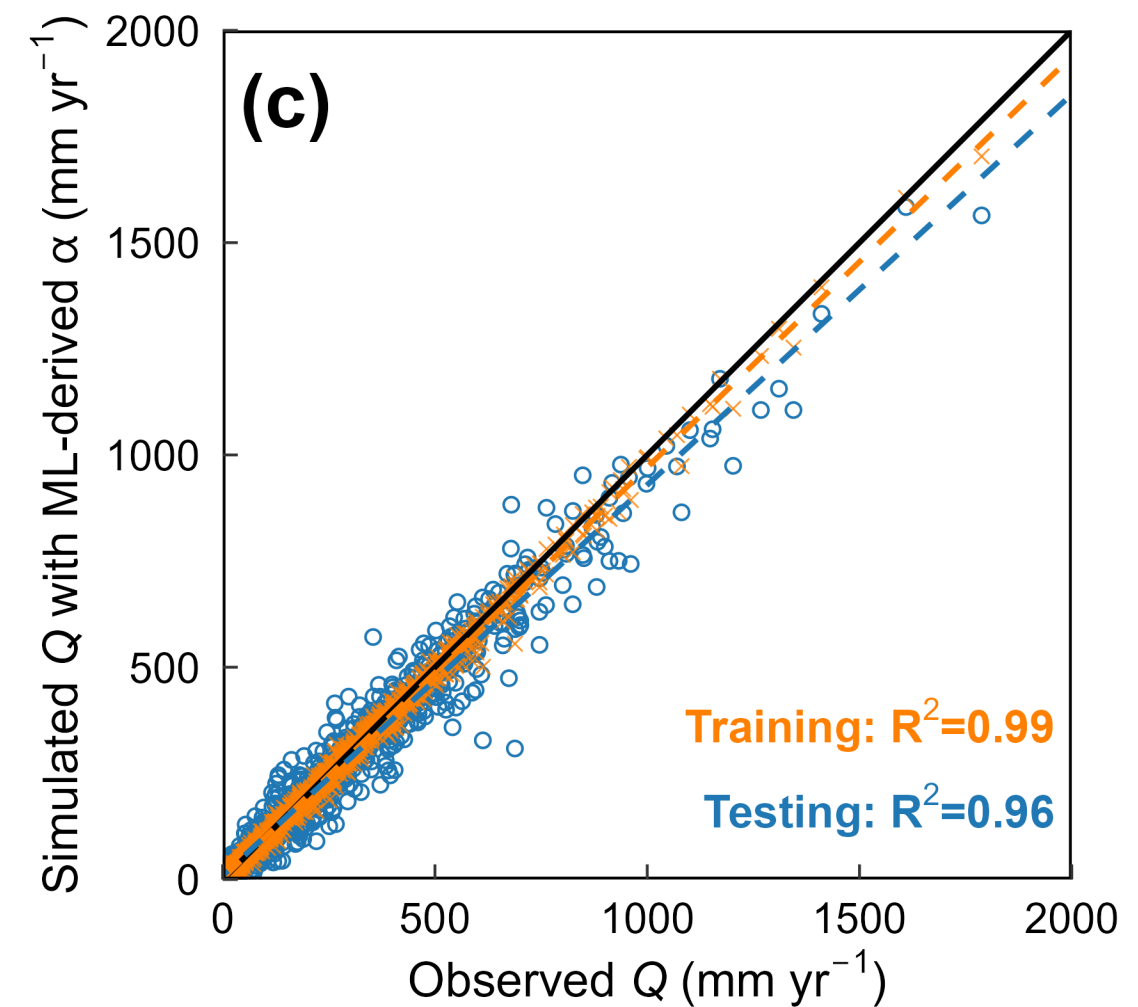
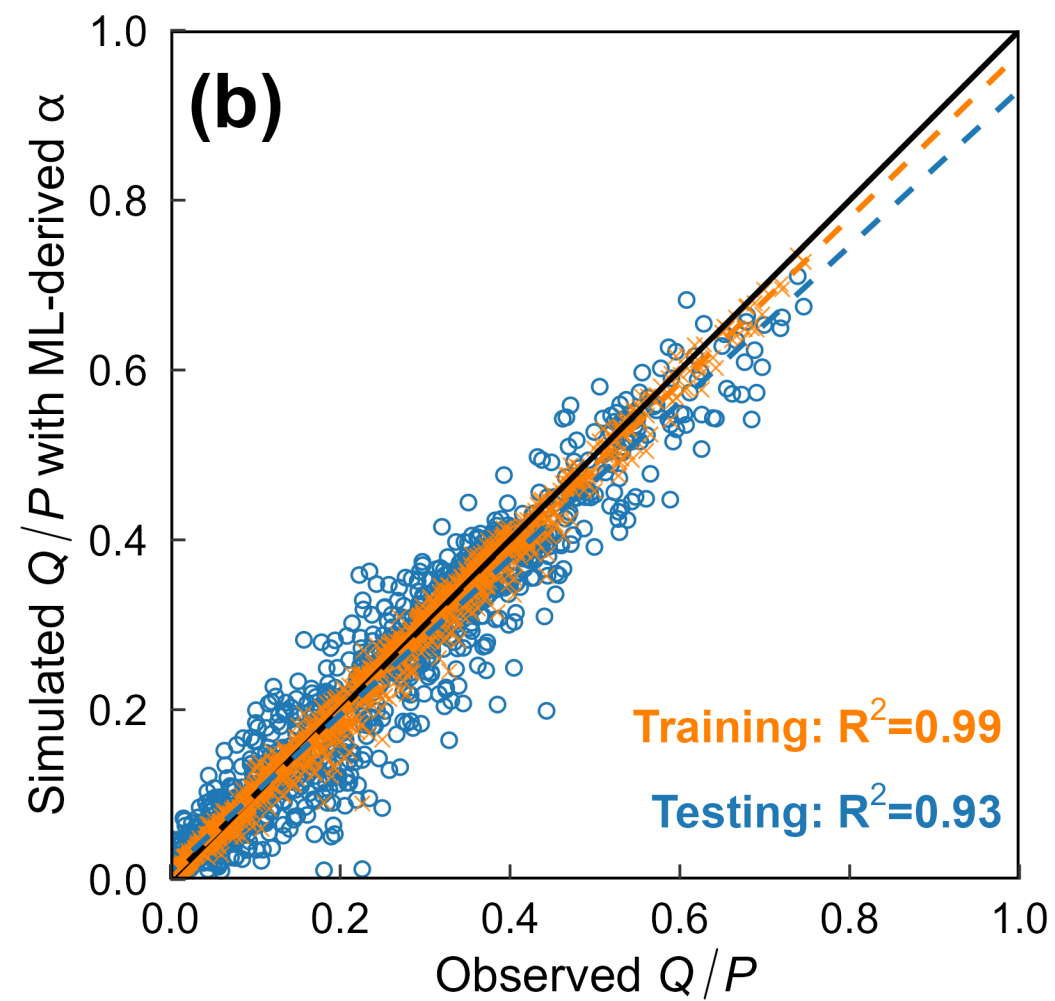
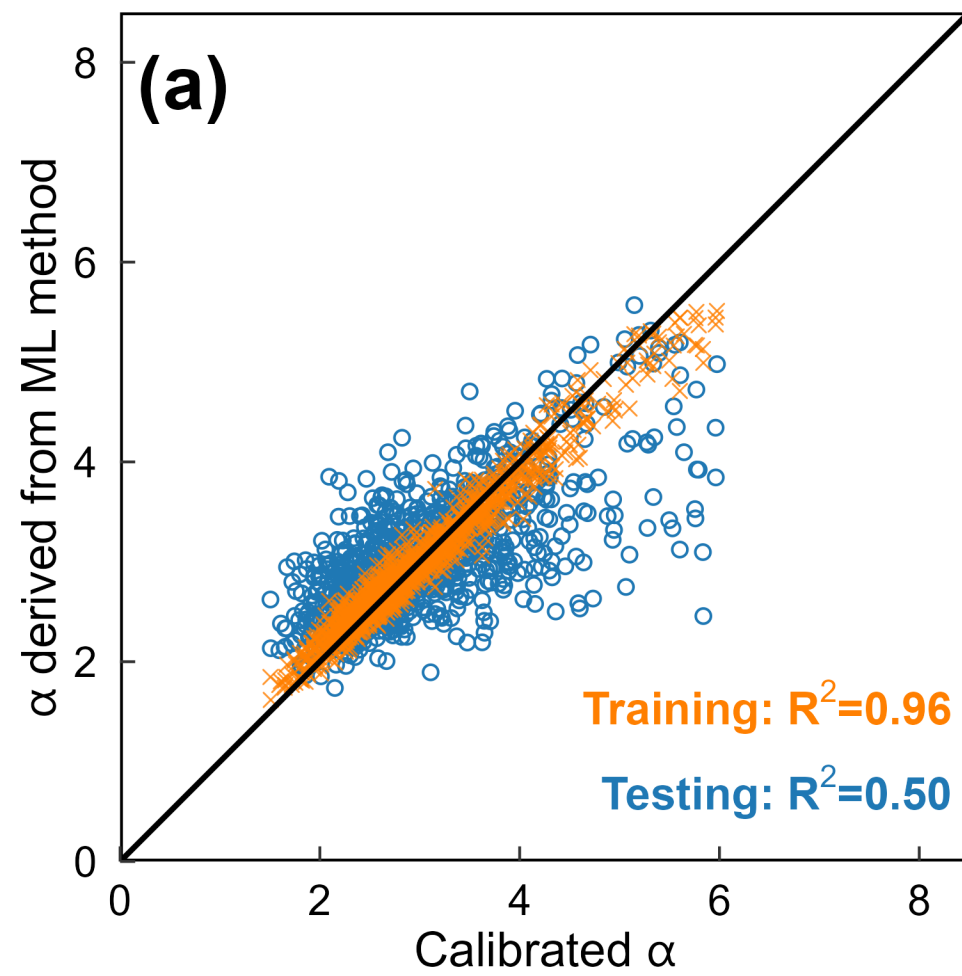


Figure5.

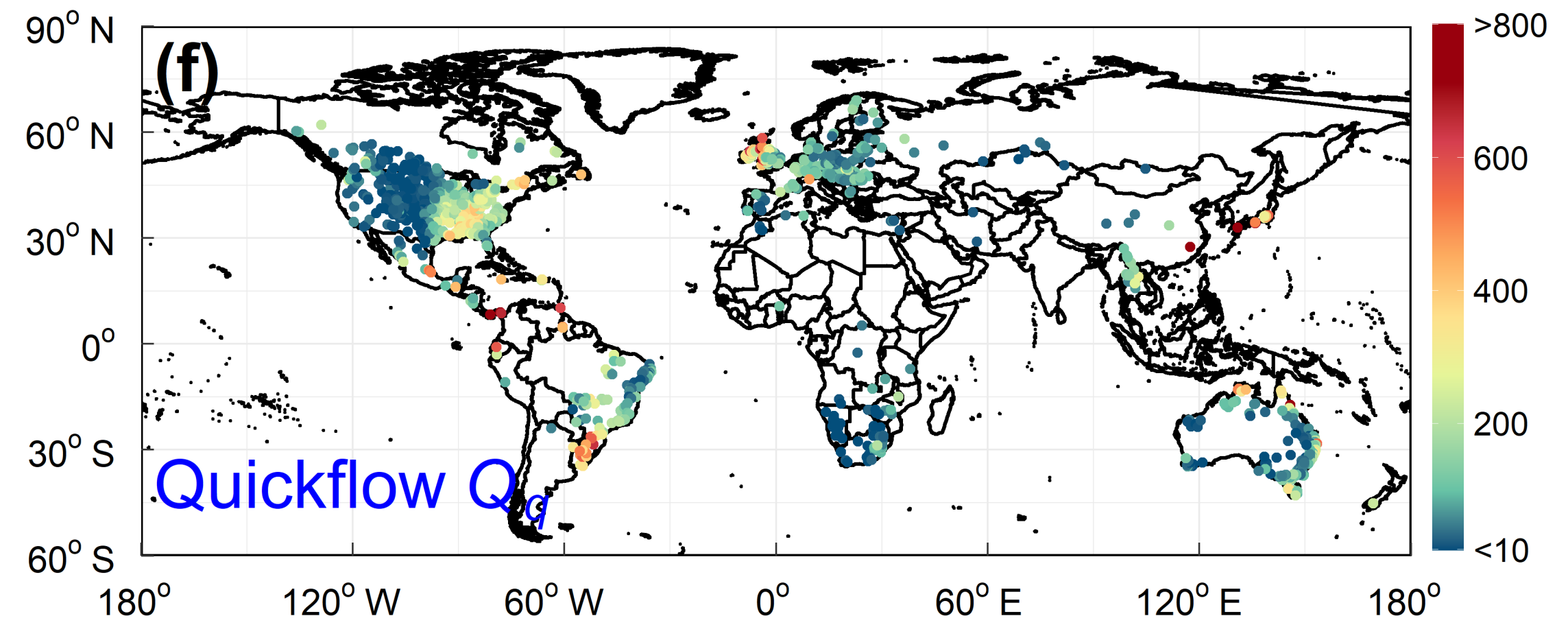
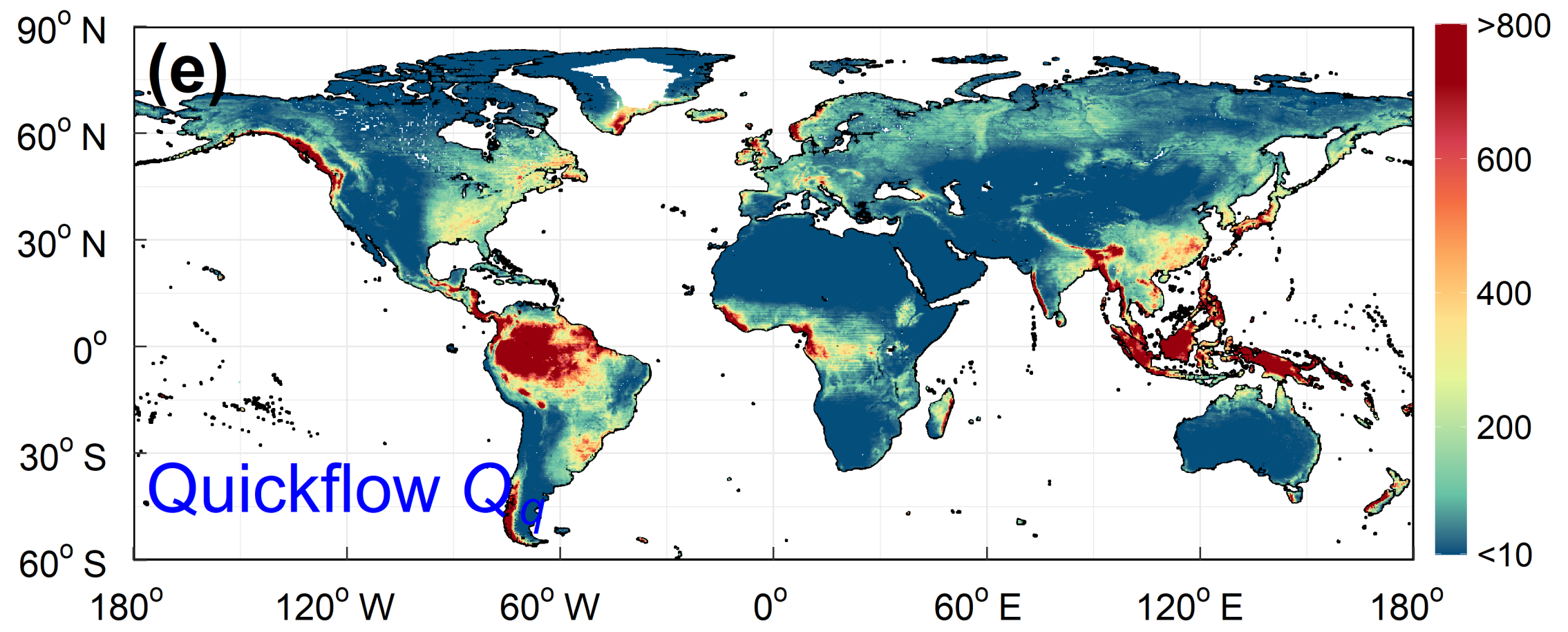
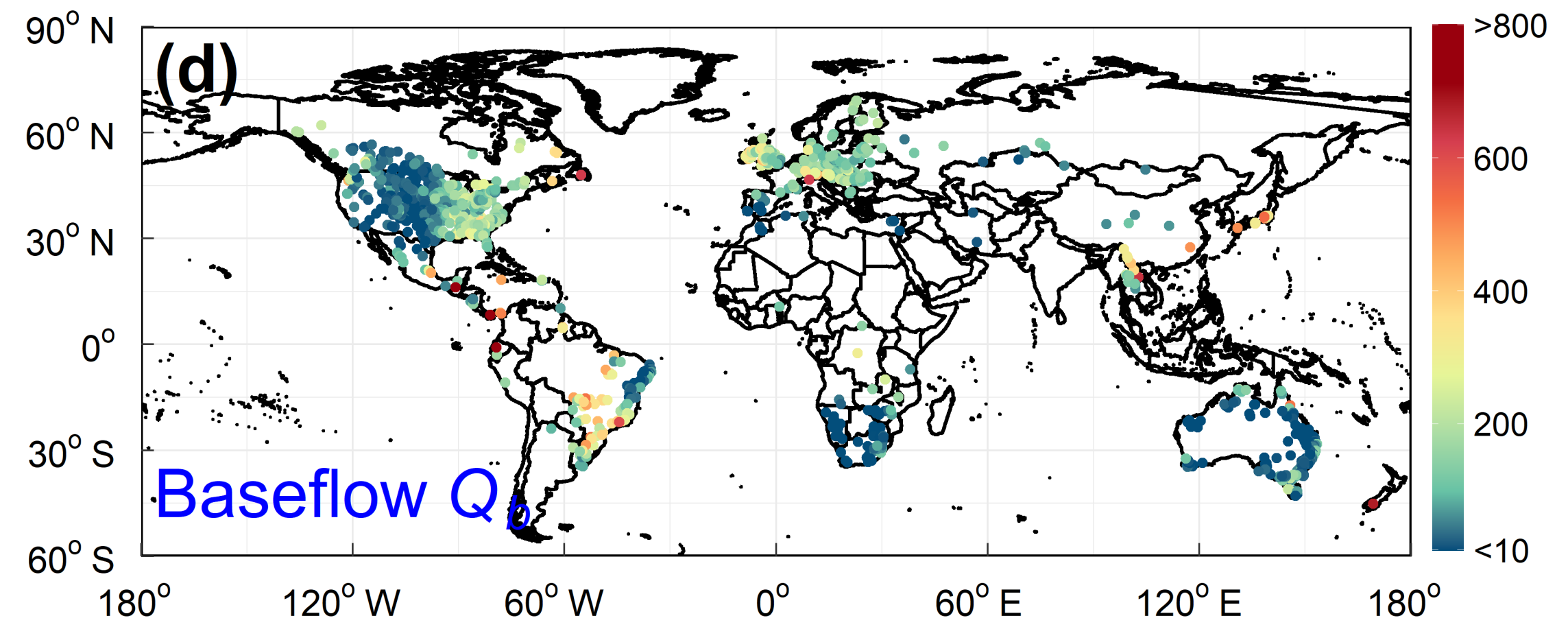
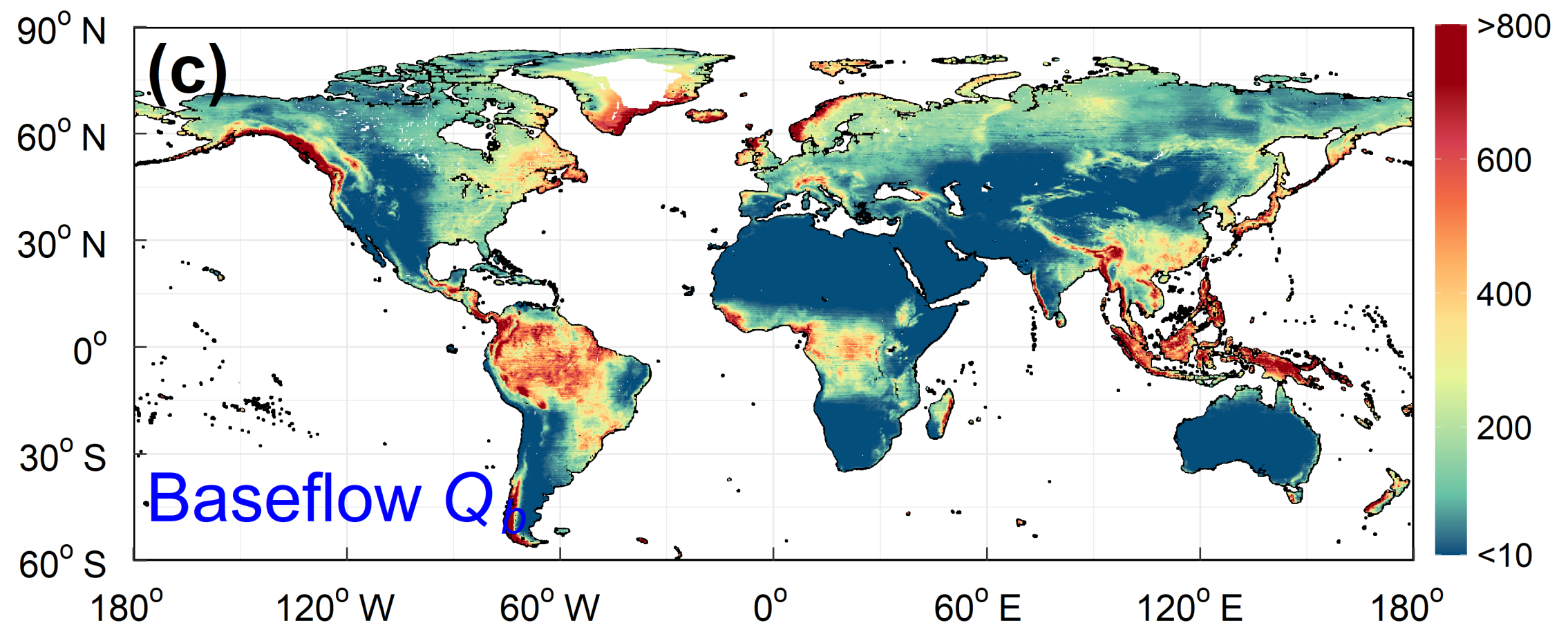
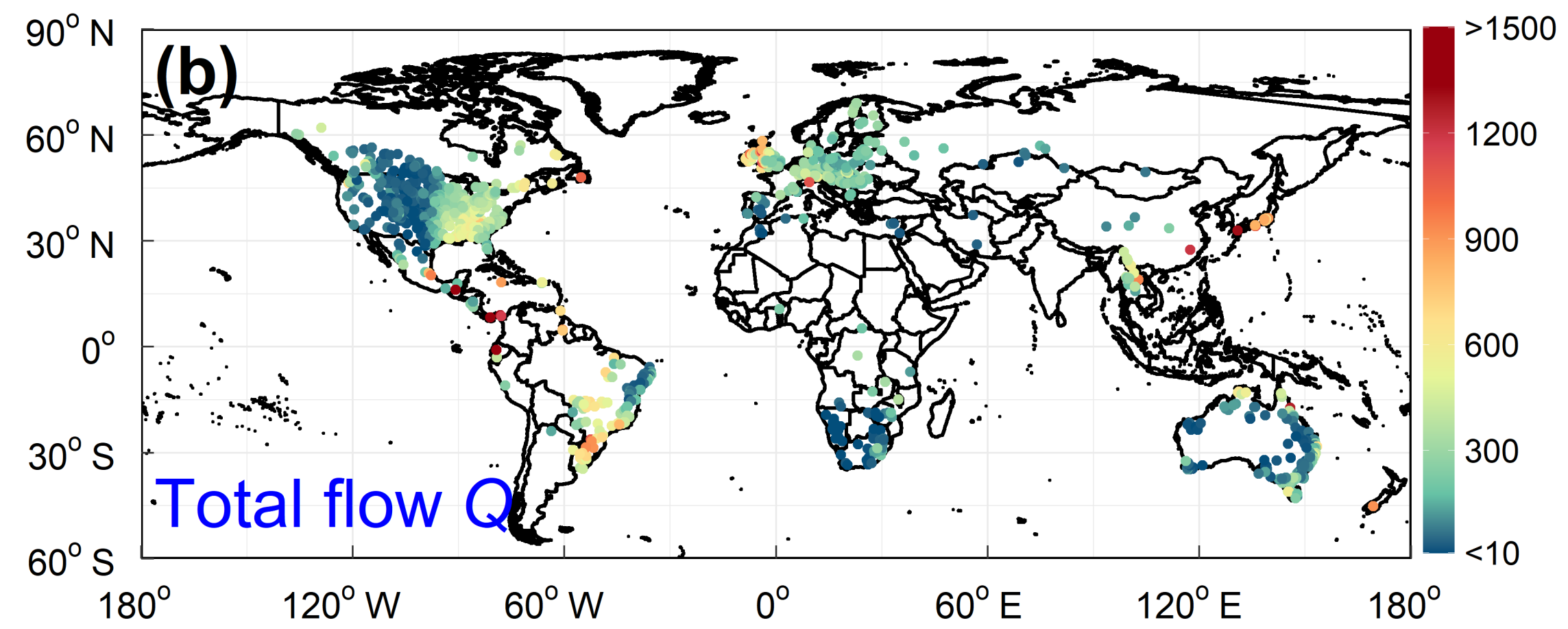
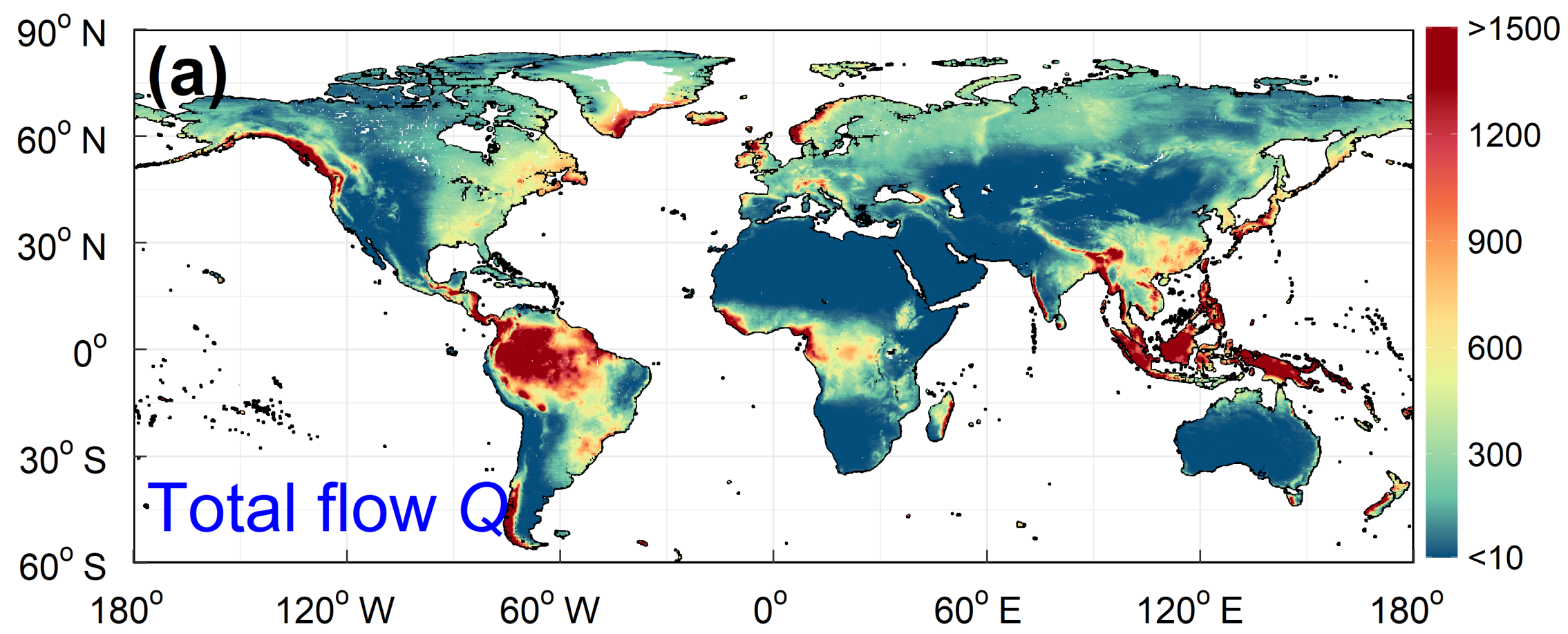


Figure6.

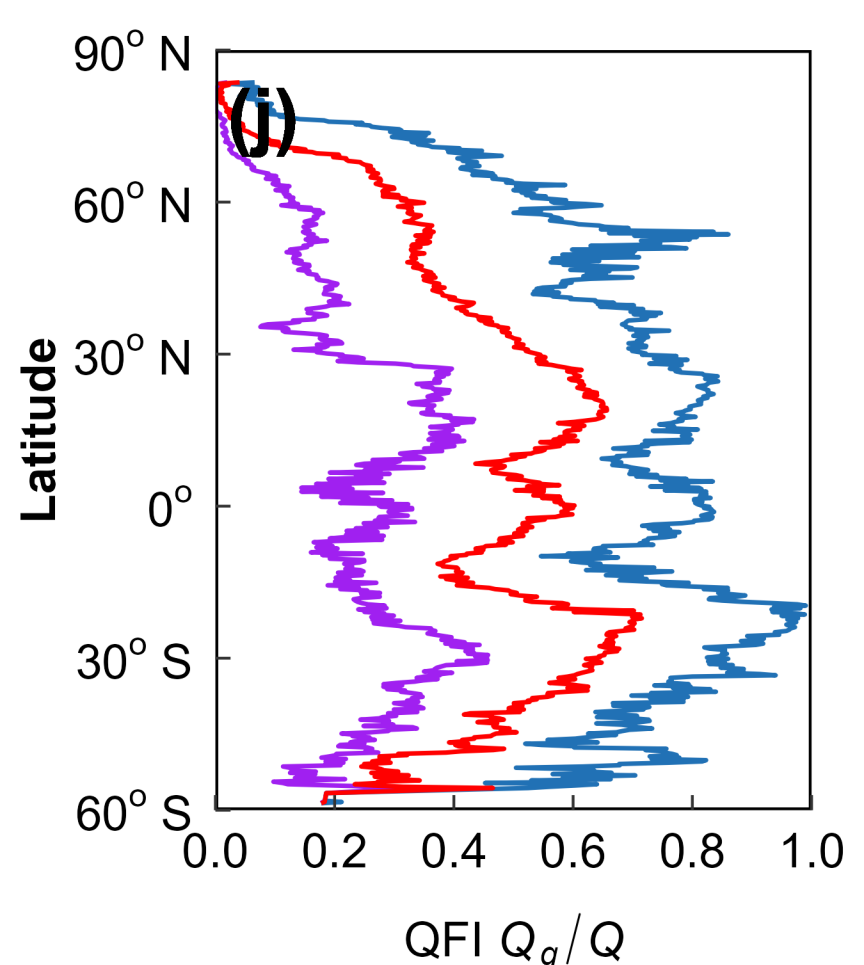
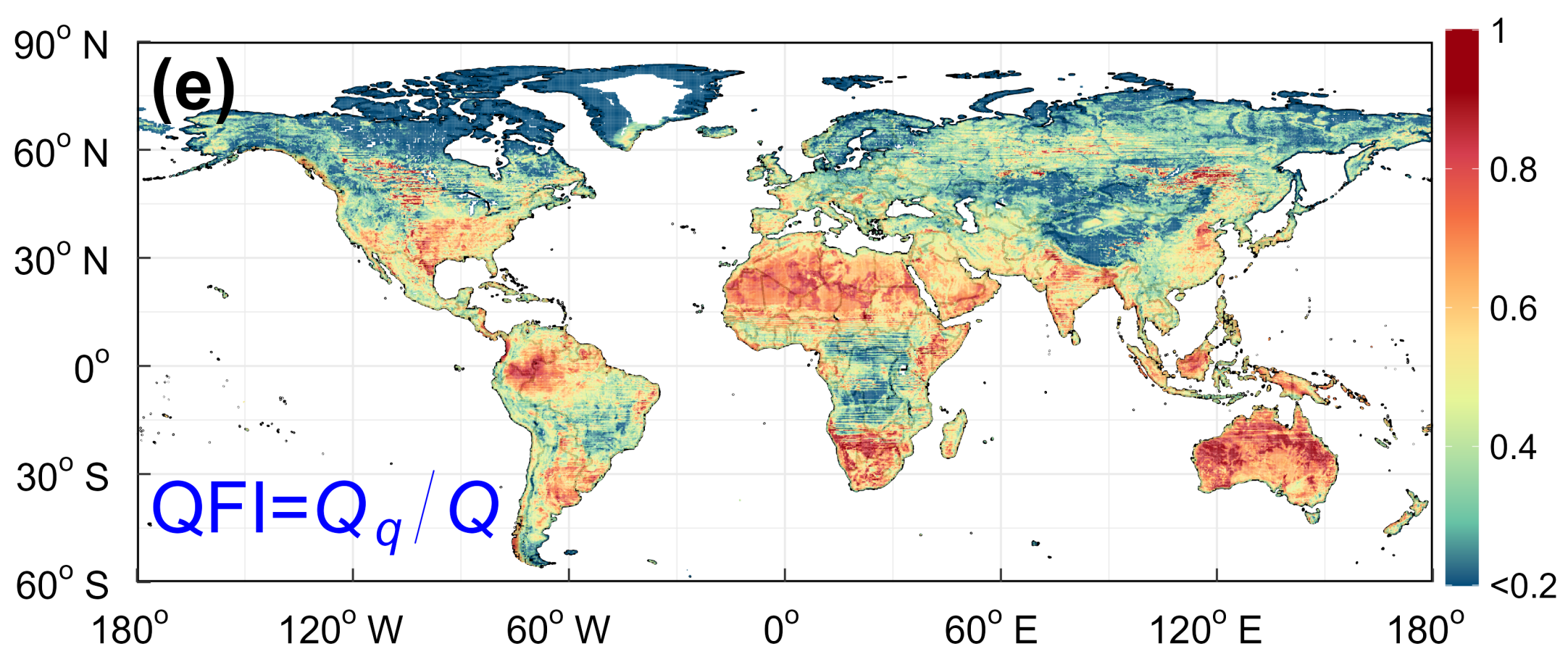
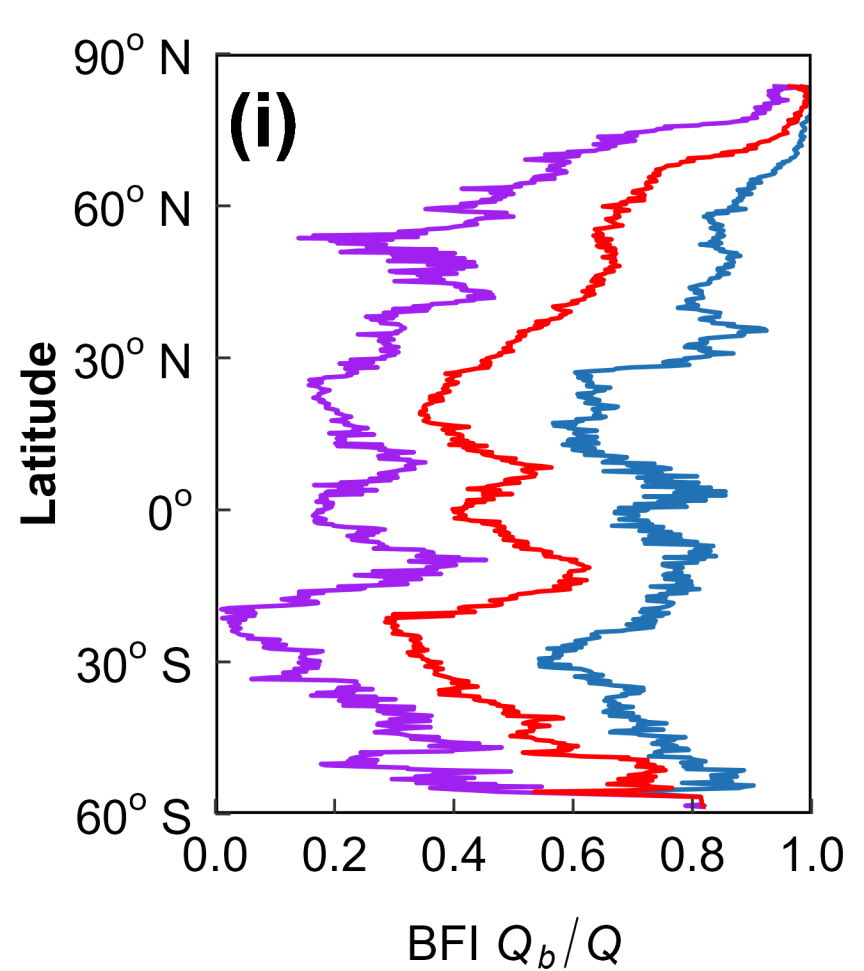
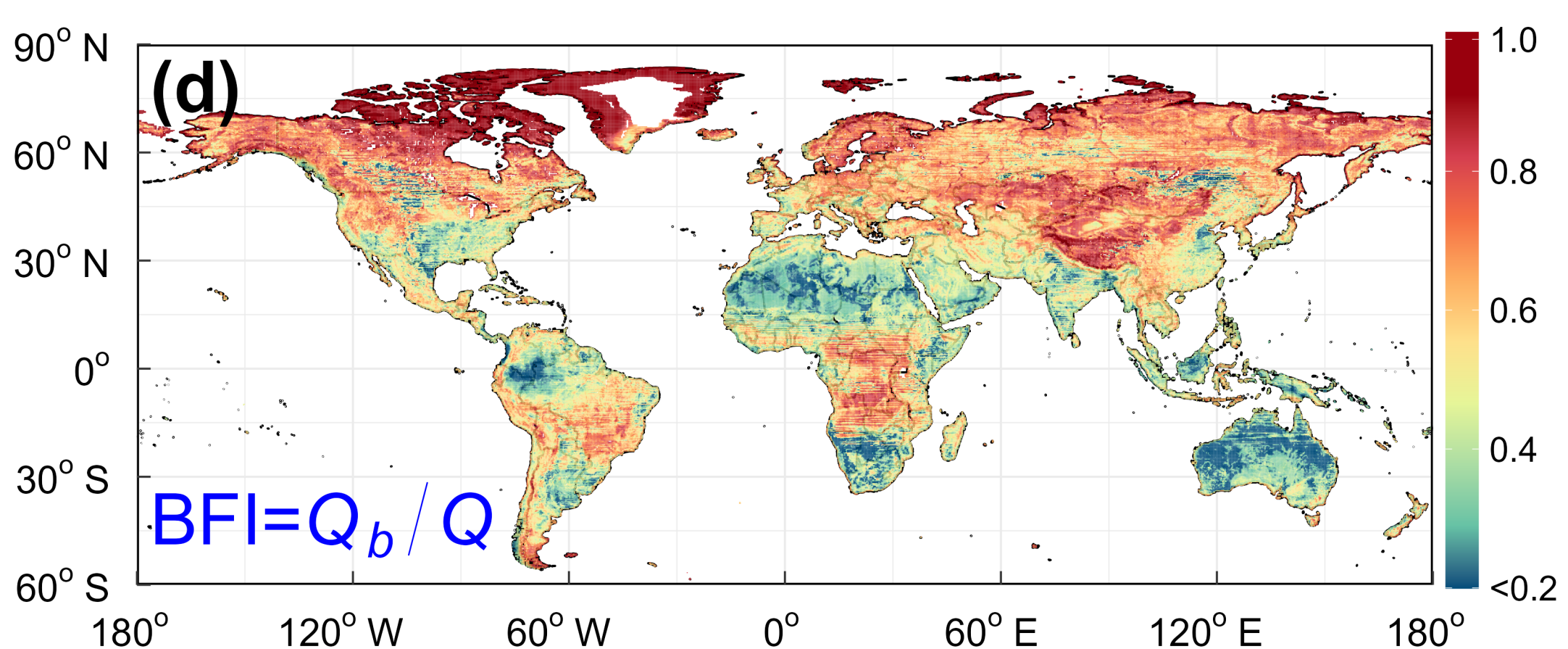
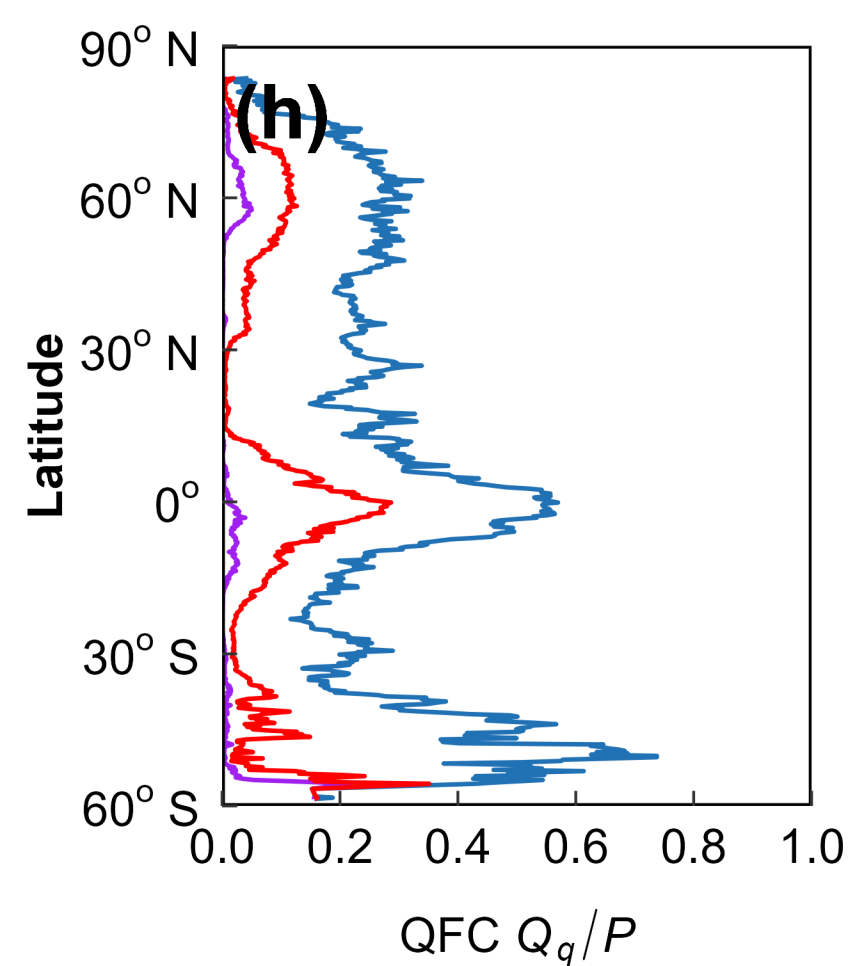
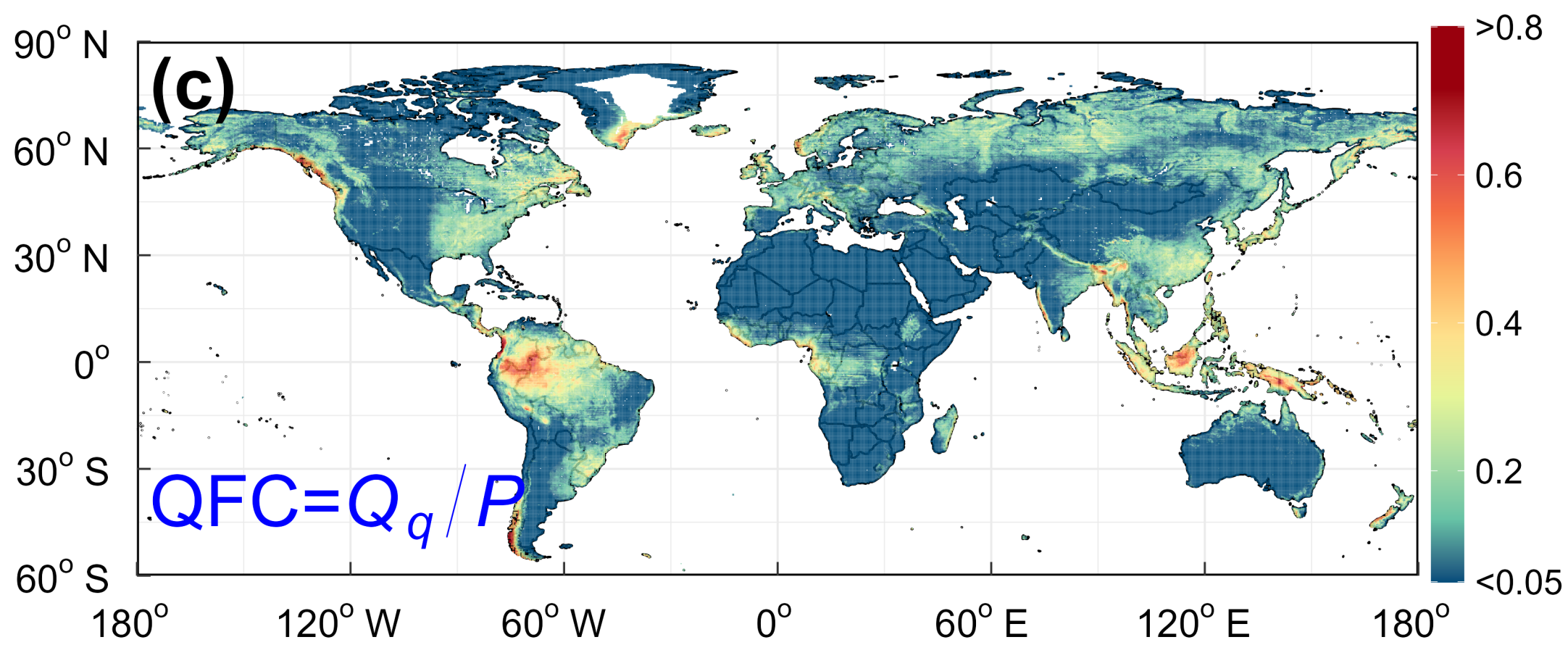
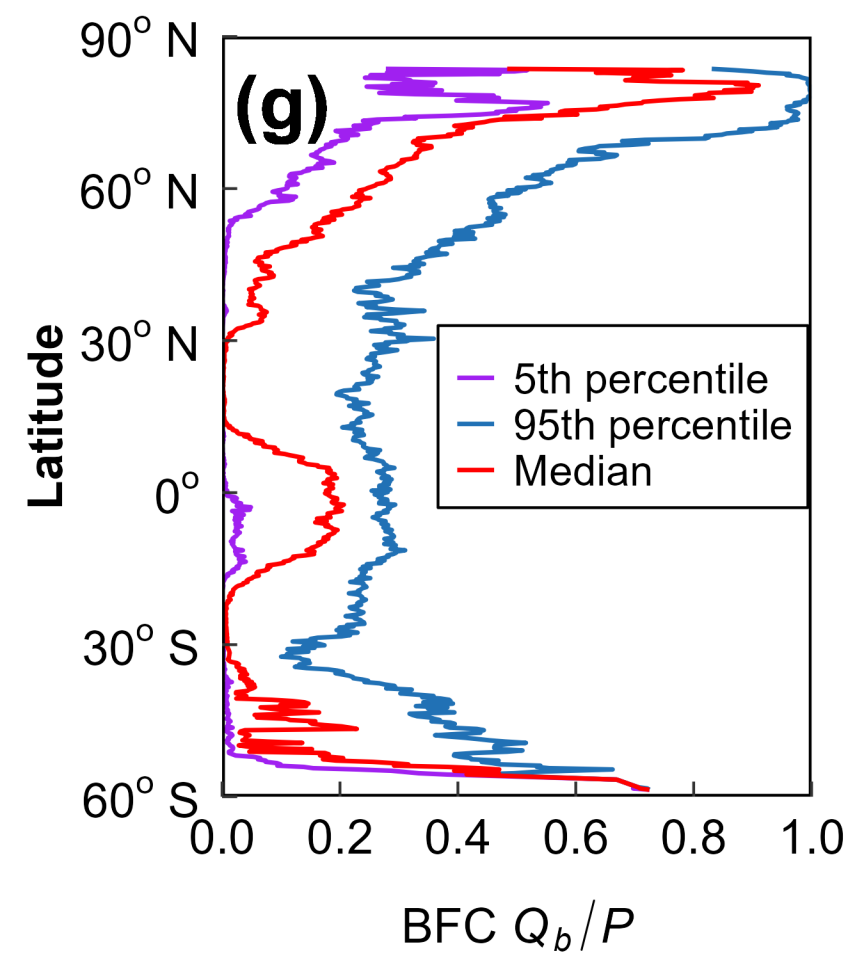
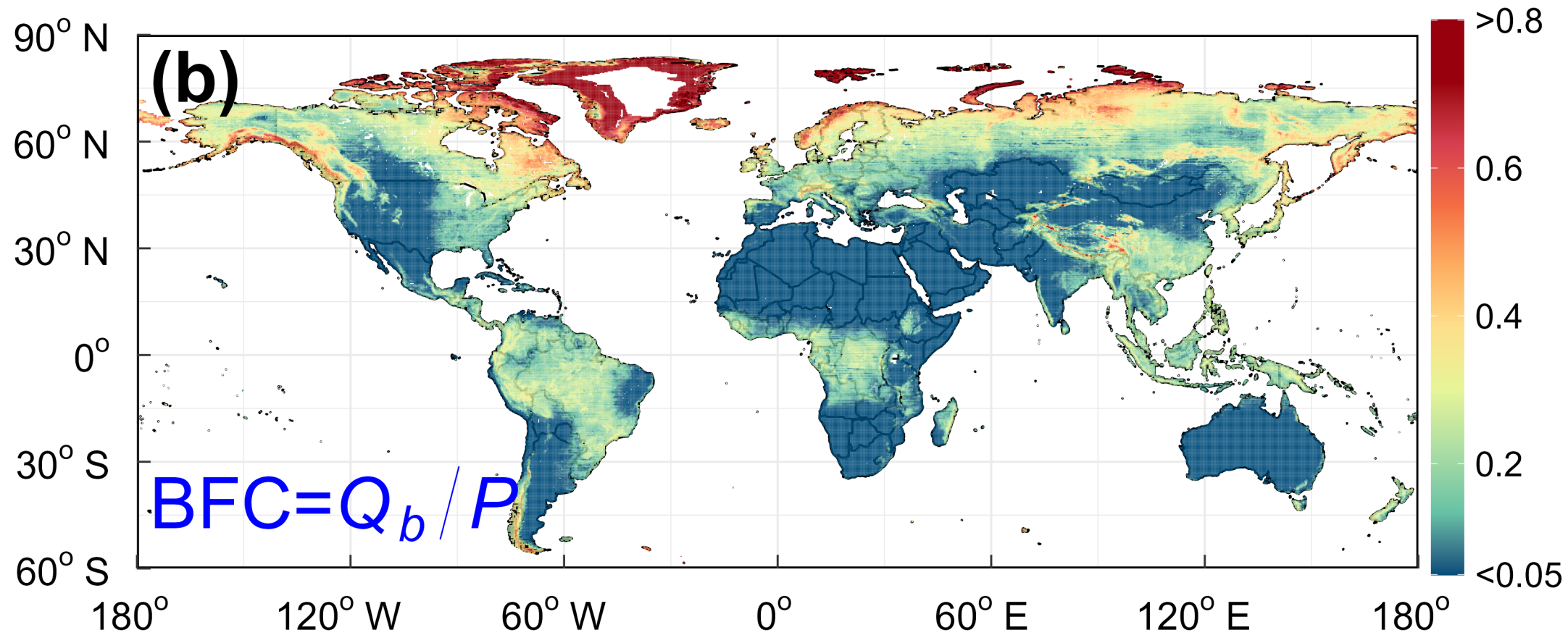
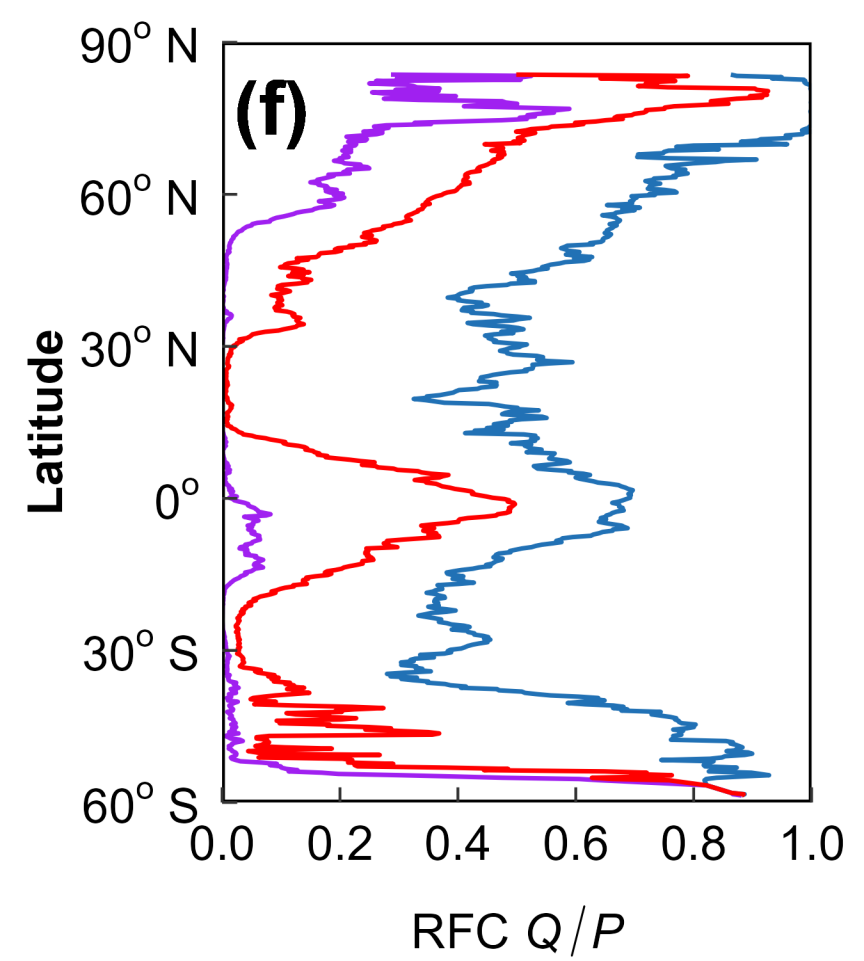
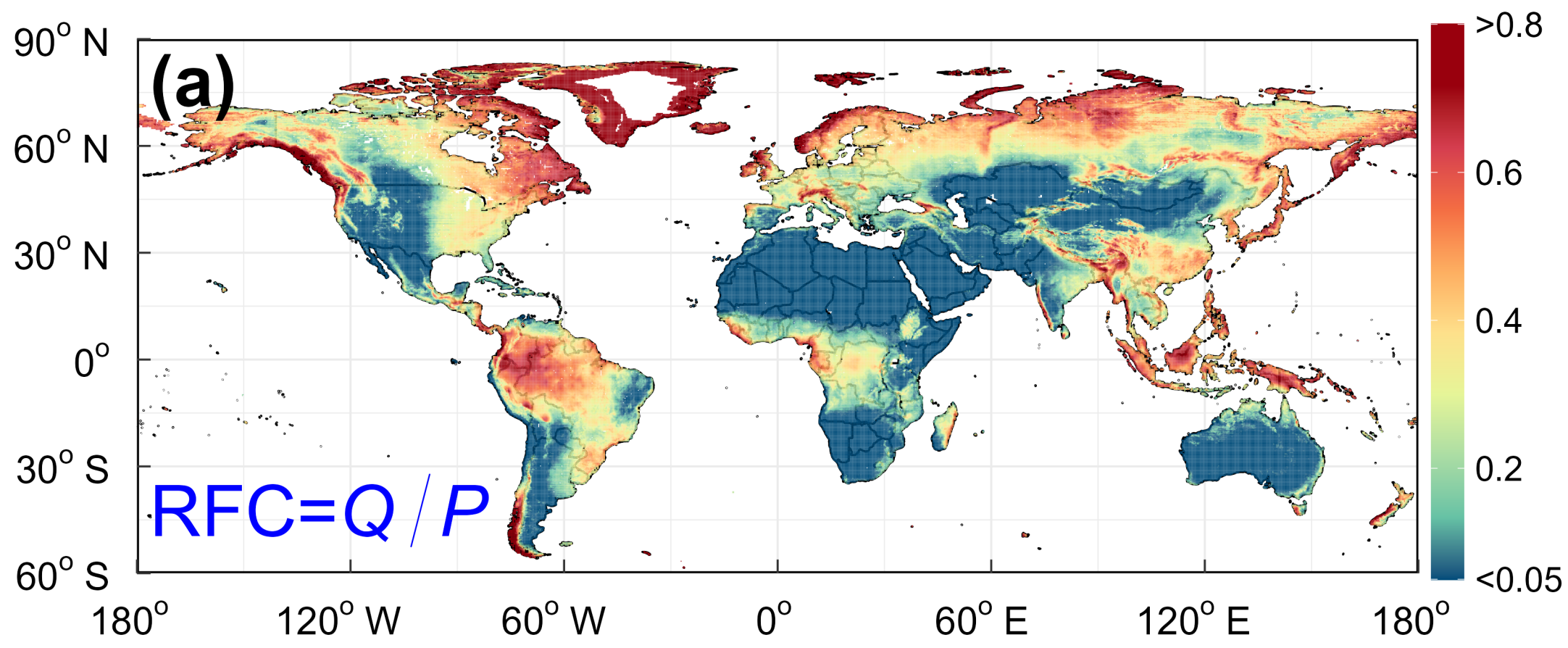
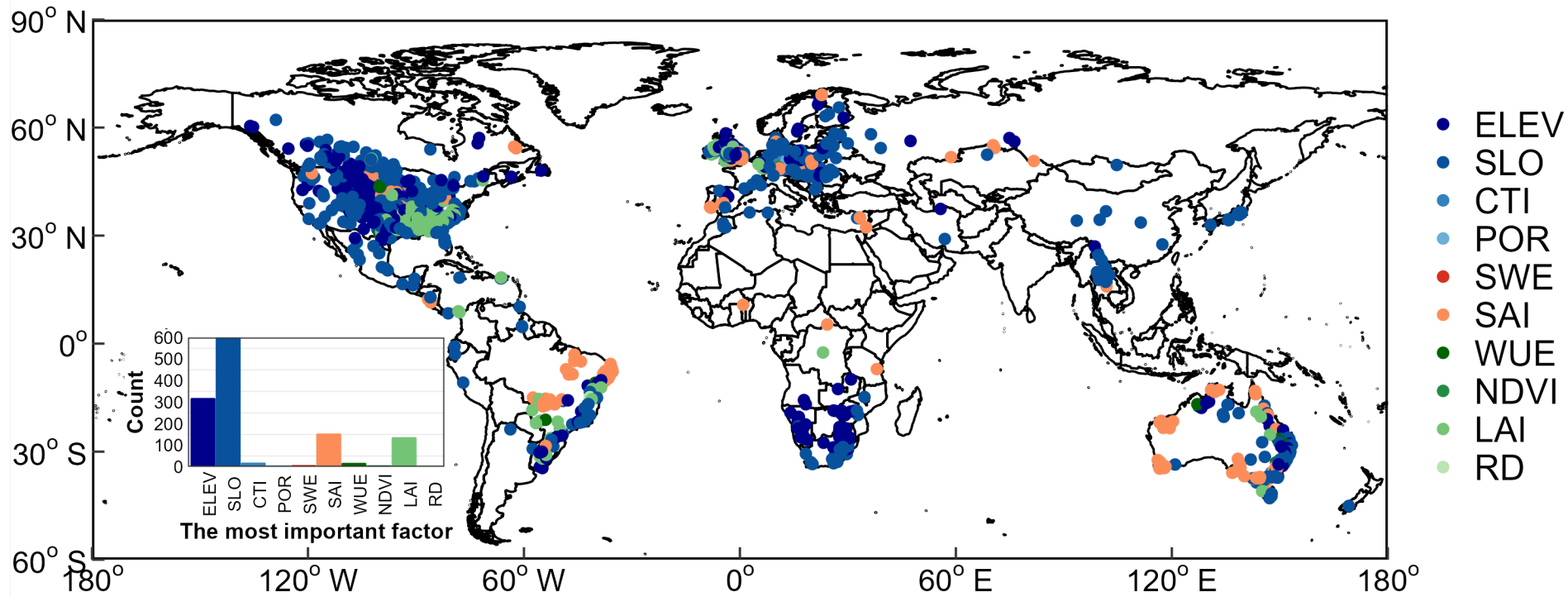


Figure7.

(a) Most important drivers for parameter α



(b) Most important drivers for parameter $Q_{b,p}$

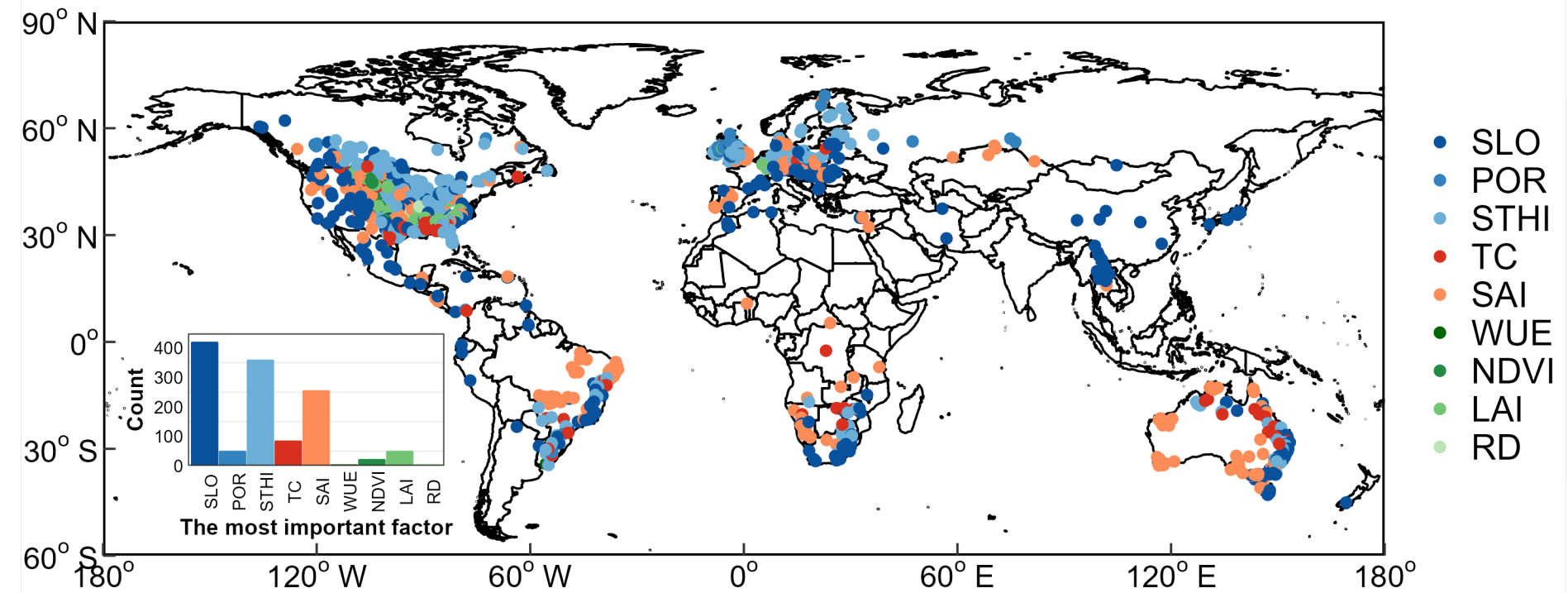


Figure8.

